Macalester Journal of Physics and Astronomy

Volume 12
Issue 1 *Spring 2024*

Article 2

May 2024

Ammonia Emission in the Milky Way Galactic Bar Dust Lanes

Charles G. Burton
Macalester College, cburton@macalester.edu

Follow this and additional works at: https://digitalcommons.macalester.edu/mjpa

 Part of the Astrophysics and Astronomy Commons, and the Physics Commons

Recommended Citation

Burton, Charles G. (2024) "Ammonia Emission in the Milky Way Galactic Bar Dust Lanes," *Macalester Journal of Physics and Astronomy*: Vol. 12: Iss. 1, Article 2.
Available at: https://digitalcommons.macalester.edu/mjpa/vol12/iss1/2

This Honors Project - Open Access is brought to you for free and open access by the Physics and Astronomy Department at DigitalCommons@Macalester College. It has been accepted for inclusion in Macalester Journal of Physics and Astronomy by an authorized editor of DigitalCommons@Macalester College. For more information, please contact scholarpub@macalester.edu.

MACALESTER COLLEGE

Ammonia Emission in the Milky Way Galactic Bar Dust Lanes

Abstract

The Central Molecular Zone (CMZ) of the Milky Way is a region of molecular gas within the inner few hundred parsecs of the Galaxy. This inner region of the Milky Way is hotter and more turbulent when compared with the disk of the Milky Way. Gas is thought to be funneled into the CMZ through dense gaseous dust lanes that are associated with the Galactic Bar. I studied two regions of one of these dust lanes using the NH3 inversion transitions of (J,K) = (1,1), (2,2), (3,3), and (4,4). Data has been obtained from the Green Bank Telescope targeting these transitions at ∼32" angular resolution. I present results probing the kinematic and thermal structure of our target gas clouds. I find the velocity of the pilot region gas cloud to be around 205 km s−1 as it accretes into the CMZ of the Milky Way. I also find the velocity of a gas cloud more toward the edge of this dust lane to be around 130 kms−1. When comparing the (1,1) to the (2,2) transition lines to probe temperature, I found a temperature of ∼20K (± 6.6K) for the pilot region and a temperature of ∼17K (± 6.6K) for the edge region. When comparing the (2,2) to the (4,4) transition lines I found a temperature of ∼65K (± 3.15K) for the pilot region. These values are in mutual agreement as the temperatures found in the edge region are slightly cooler than those found in the pilot region which is located at the midpoint of the dust lane. I use dendrogram analysis to analyze the multiple velocity components within each gas cloud. I also find heavy spatial coherence between the NH3 data, infrared emission, and CO data found for both regions.

Keywords

Galactic Bar, Milky Way Galactic Bar, Dust Lanes, Ammonia

Cover Page Footnote

This project would not be possible without the advising of Natalie Butterfield and Larry Morgan throughout my summer internship at the National Radio Astronomy Observatory. I am also very appreciative of all my peers at Macalester who helped me throughout my tenure there, as well as John Cannon for his mentorship.

This honors project - open access is available in Macalester Journal of Physics and Astronomy: https://digitalcommons.macalester.edu/mjpa/vol12/iss1/2

MACALESTER COLLEGE

Ammonia Emission in the Milky Way Galactic Bar Dust Lanes

by

Charles Burton

in the

Department of Physics and Astronomy

Advisors: John Cannon, Natalie Butterfield, and Larry Morgan

April 2024

MACALESTER COLLEGE

Abstract

Department of Physics and Astronomy

by Charles Burton

The Central Molecular Zone (CMZ) of the Milky Way is a region of molecular gas within the inner few hundred parsecs of the Galaxy. This inner region of the Milky Way is hotter and more turbulent when compared with the disk of the Milky Way. Gas is thought to be funneled into the CMZ through dense gaseous dust lanes that are associated with the Galactic Bar. I studied two regions of one of these dust lanes using the NH_3 inversion transitions of (J,K) = (1,1), (2,2), (3,3), and (4,4). Data has been obtained from the Green Bank Telescope targeting these transitions at $\sim 32''$ angular resolution. I present results probing the kinematic and thermal structure of our target gas clouds. I find the velocity of the pilot region gas cloud to be around 205 $\mathrm{km\,s^{-1}}$ as it accretes into the CMZ of the Milky Way. I also find the velocity of a gas cloud more toward the edge of this dust lane to be around 130 $\mathrm{km\,s^{-1}}$. When comparing the (1,1) to the (2,2) transition lines to probe temperature, I found a temperature of $\sim$20K ($\pm$ 6.6K) for the pilot region and a temperature of $\sim$17K ($\pm$ 6.6K) for the edge region. When comparing the (2,2) to the (4,4) transition lines I found a temperature of $\sim$65K ($\pm$ 3.15K) for the pilot region. These values are in mutual agreement as the temperatures found in the edge region are slightly cooler than those found in the pilot region which is located at the midpoint of the dust lane. I use dendrogram analysis to analyze the multiple velocity components within each gas cloud. I also find heavy spatial coherence between the NH_3 data, infrared emission, and CO data found for both regions.

Acknowledgements

This project would not be possible without the advising of Natalie Butterfield and Larry Morgan throughout my summer internship at the National Radio Astronomy Observatory. I am also very appreciative of all my peers at Macalester who helped me throughout my tenure there, as well as John Cannon for his mentorship.

Published by DigitalCommons@Macalester College, 2024

Contents

Abstract i

Acknowledgements ii

List of Figures v

List of Tables vi

1 Introduction 1
- 1.1 Barred Galaxies . . . 1
  - 1.1.1 Galactic Bar Formation . . . 1
- 1.2 The Milky Way Galactic Bar Dust Lanes . . . 3
- 1.3 Ammonia (NH_3) . . . 5
- 1.4 Overview . . . 7

2 Data Sources & Processing 9
- 2.1 Data Collection . . . 9
- 2.2 Data Reduction . . . 11

3 Analysis 15
- 3.1 Moment Map Analysis . . . 15
- 3.2 Dendrograms . . . 27

4 Discussion 39
- 4.1 Pilot Region . . . 39
  - 4.1.1 Velocity Discontinuity . . . 39
  - 4.1.2 Rotation . . . 40
  - 4.1.3 Comparison with Infrared Herschel Data . . . 40
  - 4.1.4 Pilot Region Column Densities and Temperature . . . 41
- 4.2 Edge Region . . . 43
  - 4.2.1 Velocity Discontinuity . . . 44
  - 4.2.2 Comparison with Infrared Herschel Data . . . 44
  - 4.2.3 Edge Region Column Densities and Temperature . . . 45
- 4.3 Dendrogram Analysis . . . 46

5 Conclusion 49

A Observation List **51**

Bibliography **52**

List of Figures

1.1 NGC 1300 . . . 2
1.2 Milky Way Dust Lanes . . . 4
1.3 Example NH_3 spectrum . . . 8

2.1 Example RFI . . . 12
2.2 Select pilot region channel maps . . . 14

3.1 Example midpoint spectrum . . . 15
3.2 Pilot moment 0 . . . 17
3.3 Edge moment 0 . . . 18
3.4 Pilot moment 1 . . . 19
3.5 Edge moment 1 . . . 20
3.6 Pilot moment 2 . . . 21
3.7 Edge moment 2 . . . 21
3.8 Pilot moment 8 . . . 22
3.9 Edge moment 8 . . . 23
3.10 Pilot NH_3 (1,1) Column Density . . . 24
3.11 Pilot NH_3 (2,2) Column Density . . . 25
3.12 Pilot NH_3 (3,3) Column Density . . . 26
3.13 Pilot NH_3 (4,4) Column Density . . . 27
3.14 Edge NH_3 (1,1) Column Density . . . 28
3.15 Edge NH_3 (2,2) Column Density . . . 29
3.16 Pilot cold temperature . . . 30
3.17 Pilot warm temperature . . . 31
3.18 Edge cold temperature . . . 32
3.19 Example dendrogram . . . 32
3.20 Pilot dendrogram map . . . 33
3.21 Pilot dendrogram structures . . . 34
3.22 Edge dendrogram map . . . 36
3.23 Edge dendrogram structures . . . 37

4.1 Pilot Infrared . . . 42
4.2 Pilot Infrared with CO . . . 43
4.3 Edge Infrared . . . 45
4.4 Edge Infrared with CO . . . 46

A.1 Image showing the layout of the K-band Focal Plane Array containing the 7 constituent beams. . . . 51

List of Tables

2.1 Table displaying specific line transitions and associated rest and observed frequencies. The angular resolution is calculated using the 100m effective diameter of the GBT. This is a list of all of the lines for the pilot region study, whereas in the edge region study only NH_3 (1,1), NH_3 (2,2), and NH_3 (3,3) were observed. 9

3.1 Half of the available structure properties of the pilot region. These values were found through the processing of the NH_3 (1,1) velocity cube through the astrodendro program to compute position-position-velocity statistics. 34

3.2 The rest of the available dendrogram structure properties of the pilot region. These values were found through the processing of the NH_3 (1,1) velocity cube through the astrodendro program to compute position-position-velocity statistics. 35

3.3 Half of the available structure properties of the edge region. These values were found through the processing of the NH_3 (1,1) velocity cube through the astrodendro program to compute position-position-velocity statistics. 35

3.4 Half of the available structure properties of the edge region. These values were found through the processing of the NH_3 (1,1) velocity cube through the astrodendro program to compute position-position-velocity statistics. 38

Published by DigitalCommons@Macalester College, 2024

CHAPTER 1: Introduction

1.1 Barred Galaxies

Galactic bars are known to have key roles in the process of galactic evolution (Debattista et al. 2017) by creating strong inflows of gas and dust towards the centers of their host galaxies (Athanassoula 1992). These bars are typically found in spiral galaxies, which are characterized by their flattened disk morphology and spiral arms of dust that give rise to star-forming regions (see Figure 1.1). Among more massive spiral galaxies in the optical ($M > 10^{9.6}$ $M_{\odot}$), around 30% show bars in their structure, making them extremely common (de Vaucouleurs 1964). More recent studies find that when observing in the near-infrared H-band, around 60% of galaxies are strongly barred (Eskridge et al. 2000). This disparity most likely comes from the fact that the infrared shows the more dominant older stellar population vs. the optical being affected by bright younger blue stars and dust. More recently, the literature has confirmed that bars in spiral galaxies are a sign of maturity (Sheth et al. 2008). This helps astronomers use galactic bars as a possible reference to find out at what point in the galactic evolutionary process a specific galaxy resides. When restricting our observations more locally ($z \sim 0.1$) around 65% of luminous spiral galaxies contain bars. Whereas out at redshift $\sim$0.84 this fraction drops to around 20% (Sheth et al. 2008). Studying galactic bars and their impact on gas flows, star formation, and AGN accretion is therefore very useful due to the regularity with which galaxies contain bars.

1.1.1 Galactic Bar Formation

How galactic bars form and evolve is still a topic that is being consistently researched. Research on galactic bars first started with topics on geometry and stability. Randers (1942) discusses how discovering the stability of barred galaxies will lead to the discovery of how galaxies evolve over time. If the bars are stable then one can assume that as galaxies evolve to form bars then they stay

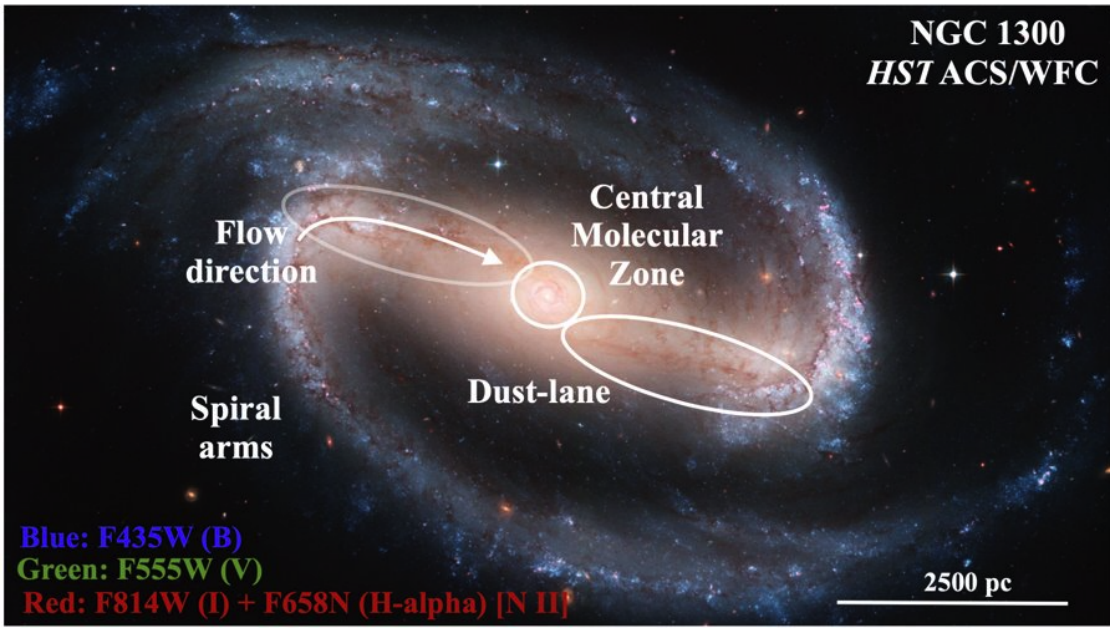

FIGURE 1.1: Schematic diagram showing the dust lane features in the barred Galaxy NGC 1300. These features transport the gas from the spiral arms toward the central molecular zone. The background Hubble image was created using F435W (B), F555W (V), F814W (I), and F658N (H-alpha) filters (Fisher & Drory 2008).

in this state for a large portion of their lives (Randers 1942). This idea would make barred galaxies some of the oldest galaxies. The other option of course is that these galaxies are unstable. This means that bars in galaxies represent an evolutionary stage in a galaxy's lifespan. This idea lets astronomers better contextualize the stability of barred spiral galaxies. The stable state of galactic bars is thought to be the main reason why they form. The main work first commenting on this stability was Ostriker & Peebles (1973). Ostriker & Peebles (1973) used N-body simulations to follow stellar orbits within an initially balanced rotating disk given an initial velocity dispersion from Toomre (1964). The main conclusion of these simulations found the stellar orbits to become unstable quite quickly. Then, this instability causes a bar to form, creating a stable axis-symmetric disk with an overall velocity dispersion much bigger than that from Toomre (1964). The big picture is that given a specific set of instabilities, the galactic bar formation process results due to the lower internal kinetic energy the bar system stabilizes in.

Another approach to the question of bar formation lies within tidal interactions.

Not to say that bars are outright formed by these tidal interactions, but that there may be an effect from tidal forces that stimulate bar formation. Miwa & Noguchi (1998) discusses that there are two types of possible tidally formed bars. The first option happens when the tidal interaction is relatively weak. This weak interaction merely spurns or activates the bar formation. The properties of the bar are then characterized by the structure of the galaxy that is being studied. The other tidal interaction is that of a close and strong interaction. In this case, the internal structure of the host galaxy is fully rearranged and the bar characteristics are determined by the kinematics of the tidal interaction. Peschken & Łokas (2019) says, using a simulation called Illustris, that most barred galaxies are formed from tidal interactions or mergers rather than that of secular evolution. This topic is still heavily debated, however.

1.2 The Milky Way Galactic Bar Dust Lanes

Within our own Milky Way Galaxy, the evidence to suggest the presence of a galactic bar has been around since at least the 1960s (de Vaucouleurs 1964). The transport of gas into the inner regions of galaxies plays a role in their evolution (Debattista et al. 2017) and their enrichment of the intergalactic medium (IGM) as discussed in the previous section. Dust lanes are observed within galactic bars such as those seen within NGC 1300 in Figure 1.1. Gas is accreted into the center of galaxies via these dust lanes, which define one step in the galactic cycle of gas inflows and outflows, and star formation. The formation of this bar happened around 8 Gyr ago (Bovy et al. 2019) when a decrease in turbulence in the disk of the galaxy allowed a state of bar stability. The age of the bar was found due to specific abundance ratios and metallicities matching more closely to those stars out in the disk of the galaxy, in comparison with those younger stars in the bulge of the Milky Way.

The Milky Way's galactic center is suggested to be fueled by gas accreting via these dust lanes (Figure 1.2)(Sormani & Barnes 2019). In Figure 1.2 the top panel shows how the dense gas in the Milky Way appears from our perspective. We reside within the plane of the galaxy, therefore just taking a continuum image

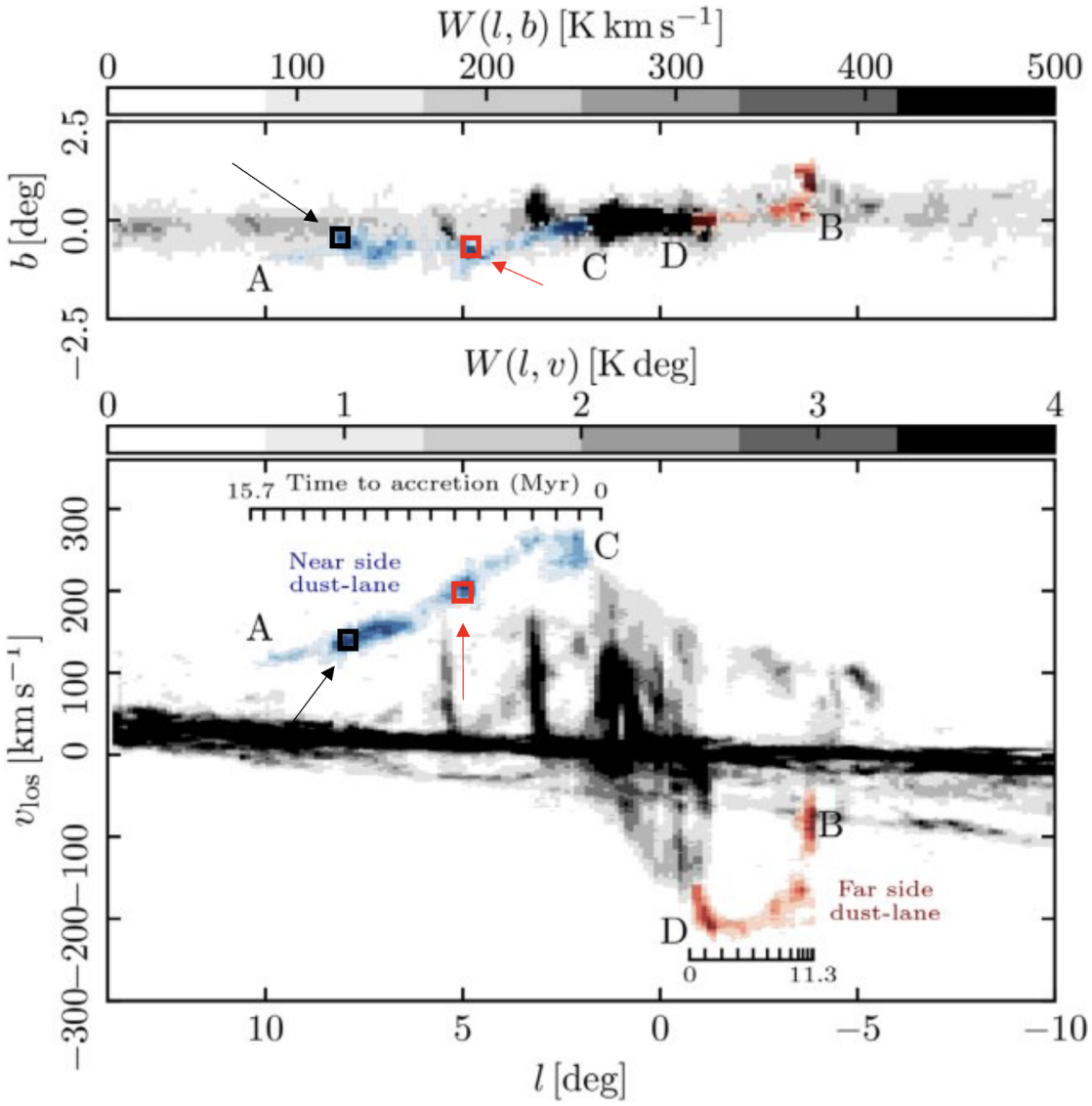

FIGURE 1.2: The Milky Way dust lanes identified in CO emission $(l, b, v_{\rm los})$ datacubes (Sormani & Barnes 2019) are highlighted in blue and red. The red box shows the location of the dense gas detected at the midpoint of the Bar and the black box shows the area detected towards the edge of the Bar.

of the galactic center does not reveal much at first glance. The only way to see the dust lanes distinctly is to look within position-position-velocity space, as shown in the lower panel of Figure 1.2. When discussing velocities for the rest of this paper I am discussing v_{los}, the velocity along our line of sight. This value is not exactly how fast or slow the gas is accreting into the center of the galaxy due to the position at which the Sun resides in comparison to the dust lanes. In this figure, the dust lanes stand out as highlighted in blue for the near-side dust lane,

and in red for the far-side dust lane. This accretion through the dust lanes is said to be episodic as the inflow rate is variable with time (Sormani & Barnes 2019). We can see this in Figure 1.2 as the brighter points of emission for the near-side dust lane fall off into more dim emission regions, and then become bright again. According to Sormani & Barnes (2019) the location labeled by the red arrow and box in Figure 1.2 is set to reach the galactic center in around 6 Myr and the region in the black box in around 12 Myr. Other than, inflow rate, outflow rate, and accretion, studying the galactic bar dust lanes will help figure out how much of the mass of the dust lanes is feeding star formation processes in the galactic center (Kruijssen et al. 2014), and if star formation is even realistic in turbulent systems such as these.

The two clouds I studied in this project are noted in Figure 1.2 within the red and black boxes. I used NH_3 emission to study both of these regions. The region within the red box will hereafter be called the pilot region of the dust lanes, and the region within the black box will be called the edge region of the dust lanes. The pilot region has a known velocity of v_{los} ~210 $\mathrm{km\,s^{-1}}$ and the edge region has a known velocity of v_{los} ~140 $\mathrm{km\,s^{-1}}$ (Sormani & Barnes 2019).

1.3 Ammonia (NH_3)

Astronomers have been using NH_3 to study the interstellar medium since its discovery within the interstellar medium (ISM) in 1968 (Cheung et al. 1968). This 1968 paper discovered NH_3 emission towards the galactic center in the J=1 and K=1 rotational levels. Later, Ho and Townes followed up this discovery by determining how NH_3 can be used advantageously by observational astronomers. This was done through an explanation of the molecule's hyperfine emission structure as well as discerning column densities and temperatures of NH_3 systems (Ho & Townes 1983).

Structurally, NH_3 is a symmetrically topped molecule made up of one nitrogen atom and three hydrogen atoms bound in a trigonal pyramidal structure. When describing what state of NH_3 is being studied we discuss the J and K quantum numbers. J is the angular momentum quantum number and K is the quantum

number of the projection of the angular momentum along its axis. We define the rotational energy to be a function of these two quantum numbers J and K.

Other than rotational energy, NH_3 molecules also undergo vibrational plane switching. With the potential barrier of the hydrogen atoms being low enough, the nitrogen atom can quantum tunnel through the plane of the three hydrogen atoms releasing a photon in the radio and microwave frequency ranges (300MHz - 300GHz). As described in Ho & Townes (1983), the hyperfine structure of the NH_3 emission allows for a calculation of the column density of the system. NH_3 column density is defined as the number of beam-averaged NH_3 particles along the line of sight to the observed gas clouds. So barring any foreground sources and assuming that the targets are optically thin, the column density gives a beam-averaged number of NH_3 molecules along a line of sight. With NH_3, finding the column densities is done by taking a ratio of the brightness of the main emission line of NH_3 with the brightness of the largest hyperfine line. Hyperfine lines (as shown in Figure 1.3 from Myers & Benson (1983)) within the spectroscopic structure of NH_3 are therefore useful to the observational astronomer because of the fewer steps needed to create optical depth and temperature maps. For this paper, I used the formalism from Mauersberger et al. (2003) which is described by Equation 3.4. This formalism does not make explicit use of the ratios discussed in this section. So in comparison with other molecules, such as CO, an observer would have to collect multiple data sets of different CO transitions or with different isotopes ($_{13}$CO vs $_{12}$CO) and find the ratio between those to find the column density. NH_3 can discern this with a singular transition. More specifically, Figure 1.3 shows both observed and modeled hyperfine lines along with the residual noise found using the Haystack observatory and the 43m telescope at the National Radio Astronomy Observatory (NRAO). This figure shows the NH_3 (1,1) transition with a velocity resolution of 0.075 $\mathrm{km\,s^{-1}}$. These observed lines can be directly compared to the found NH_3 (1,1) hyperfine lines for this project, shown in Figure 3.1.

After calculating the column densities, with two or more measurements of NH_3 transitions, one can discern the temperature of the system. The ratio of the column densities of two different NH_3 transitions yields the desired temperature value and this process is similar to other molecules (Equation 3.5). Also, NH_3 has a relatively low dipole-moment meaning that it reaches thermal equilibrium with ambient gas

quickly via collisions with surrounding H_2 gas (Mills & Morris 2013). H_2 gas being the most abundant molecule in the universe means that if NH_3 is able to reach thermal equilibrium with the H_2 then I have a very good temperature tracer for the molecular clouds.

Other than the usefulness of the hyperfine structure, NH_3 is also an excellent molecule for these observations because it is a high-density gas tracer. This allows observations with NH_3 to better penetrate potential protostellar clouds (Morgan et al. 2010), due to a critical density of $\eta_{crit} = 10^4 \text{cm}^{-3}$ (Swade 1989) before it becomes thermally excited.

For the observations of this project, I study mainly the NH_3 (J,K) = (1,1)-(4,4) inversion transitions. Within the observations of the NH_3(1,1) transition, the hyperfine structure is more clearly seen due to the expected higher signal-to-noise ratio (Morgan et al. 2010). The (1,1) and (2,2) transitions are particularly important to the measurement of the temperature of the NH_3 gas within the dust lanes (Section 4). To measure the temperature of the gas I use two different NH_3 transitions. I am able to probe each transition for column densities using the optically thin case outlined in Mauersberger et al. (2003) (Equation 3.4). Then the column density ratio of the (1,1) to (2,2) transition is used to find the rotational temperature at each point (Equation 3.5). This gives us our temperature map. This process is explained more in Section 4. The temperature structure of the CMZ of the Milky Way is very complex, and NH_3 allows us to probe some of those complex qualities.

1.4 Overview

This paper outlines the use of the Green Bank Telescope (hereafter, GBT) located in Green Bank, West Virginia. The GBT is a single-dish radio telescope with an effective diameter of 100 meters. The data collection process is described in Section 2.1, along with some initial interpretations of the data cubes. The data from the GBT is then reduced, as described in Section 2.2, through a combination of automated and manual processes. Analysis of the Pilot and Edge regions is discussed in Chapter 3 by showing the emission and temperature maps of each

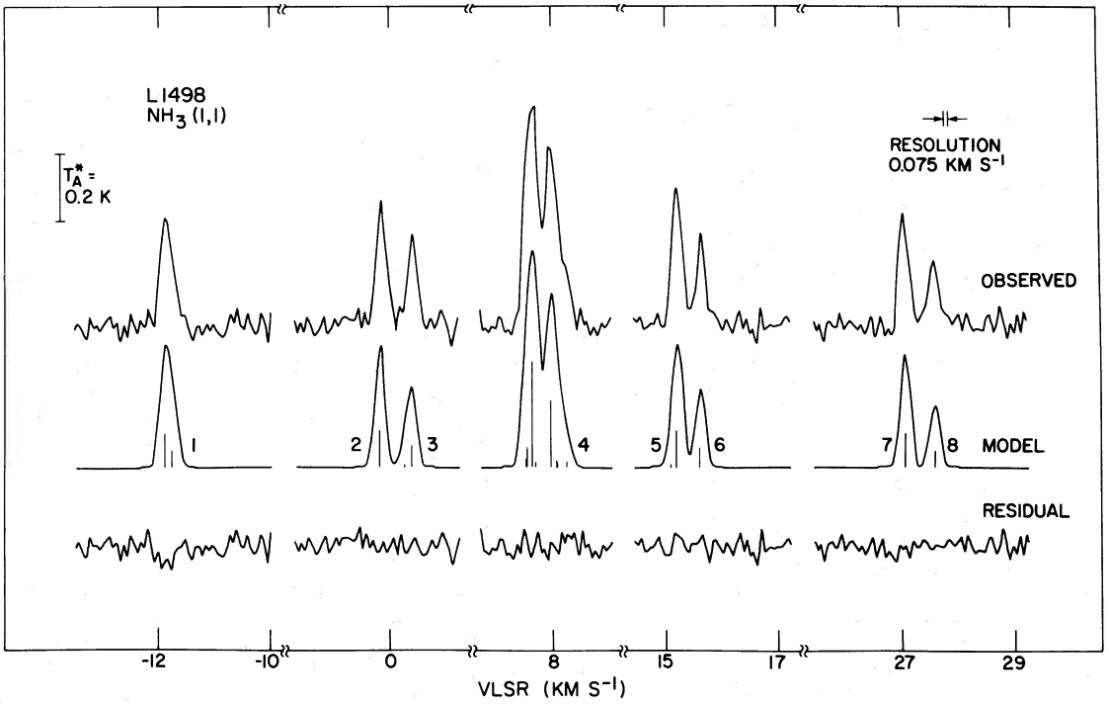

FIGURE 1.3: Example of (1,1) transition spectrum with hyperfine lines of L1498, a protostellar core from Myers & Benson (1983).

region, as well as the analysis of cloud fragmentation through dendrograms. Dendrograms are a tool used to help discern whether these two regions contain active star formation or not. The explanation and subsequent equations of each type of used moment map are described in Section 4. In Chapter 4 I discuss the findings from the analysis section and the future conclusions that can be drawn from the data.

CHAPTER 2: Data Sources & Processing

2.1 Data Collection

The GBT was used for these observations. The GBT has a 100-meter effective diameter dish and is located in Green Bank, West Virginia. To measure the NH_3, HC_5N, and HC_7N transitions the GBT K-band Focal Plane Array (KFPA) receiver was used. This receiver has a frequency range of 18.0 GHz to 27.5 GHz. The KFPA contains 7 beams as shown in A.1. The 7 beams on each line transition, listed in Table 2.1, enables a faster mapping strategy. The data was taken using On-The-Fly (OTF) mapping scans (RALongMapWithReference), which are horizontal cross-sections of the total imaging region. These scans consist of both off-scans and on-scans. Data is discretized by frequency, beam number, polarization, and integration to fully complete reductions. The observed frequencies shown in Table 2.1 have been doppler-shifted from a known rest frequency for each transition (also shown in Table 2.1). The range of frequencies between 18 and 26 GHz, known as K-band, fall within a poor atmospheric transmission regime due to water vapor. Therefore, 'dry' and stable weather conditions are necessary to observe at these frequencies. In Section 2.2 I discuss opacity values for specific frequencies which take into account atmospheric absorption in our data.

Line Transition	Rest Frequency (GHz)	Observed Frequency (GHz)	Angular Res (arcsec)
HC_7N(21-20)	23.687	23.674	31.847
NH_3(1,1)	23.694	23.681	31.838
NH_3(2,2)	23.722	23.709	31.801
NH_3(3,3)	23.870	23.857	31.604
HC_5N(9-8)	23.963	23.395	31.481
NH_3(4,4)	24.139	24.126	31.252
HC_7N(22-21)	24.815	24.802	30.400

TABLE 2.1: Table displaying specific line transitions and associated rest and observed frequencies. The angular resolution is calculated using the 100m effective diameter of the GBT. This is a list of all of the lines for the pilot region study, whereas in the edge region study only NH_3 (1,1), NH_3 (2,2), and NH_3 (3,3) were observed.

Observations were taken over six observing sessions beginning in April 2020 and ending in February 2021. Five of these observing runs targeted the center of the near-side dust lane (4.75° Galactic Longitude, 0.78° Galactic Latitude) and the sixth session targeted the edge region (8.198° Galactic Longitude, -0.596° Galactic Latitude). The bandwidth used was 23.44 MHz wide with a velocity resolution of 0.07 $\mathrm{km\,s^{-1}}$ before data smoothing. All of the data used the position switching option of the GBT which has the beam slew to an off position of the sky to background subtract any non-source emission.

The On The Fly (OTF) mapping technique was used during the data collection process with the GBT. This process is in contrast with a 'point and integrate' method which is traditionally used to map discrete positions on the sky. The use of this mapping procedure was important because of how much faster it will map the clouds that are being observed, which reduces atmospheric changes that I already have to interpolate to find (Section 2.2). Each integration was taken at a data dump time of 1.5-2 seconds. Another important note to keep in mind during setup for these observations was the sampling rate. Understanding the sampling rate and using it effectively is necessary to use the OTF technique during the mapping process. Undersampling will cause gaps within our map. This idea is explained by Nyquist Sampling. This gives a critical spacing between each of our integrations for this type of mapping that allows us to reconstruct the source. The critical spacing is given by:

$$\theta_N = \frac{\lambda_{obs}}{2D} radians \tag{2.1}$$

where D is the effective diameter of our telescope dish in meters and λ_{obs} is our observed wavelength in meters. This is the exact sampling needed for perfect reconstruction, but in practice, the data is slightly oversampled to bypass any errors within scans that might hinder data compilation. This critical spacing is different for each of the observed frequencies, so the data has to be taken with regard to the smallest critical spacing to avoid gaps in the data. The value of the smallest critical spacing is the data taken at 24.802 GHz which gives a critical spacing of 12.47 arcsec. Now with our critical spacing, I can solve for our sampling rate. The sampling rate also takes into account our system's data dumping time. This is the time of each integration on the sky and the time for the spectrometer

to "dump" that data. The sampling rate is given by:

$$R(arcsec/s) = \frac{\theta_N}{n_{os} t_{dump}} \tag{2.2}$$

where t_{dump} is our data dumping time in seconds, θ_N is our critical spacing given in Equation 2.1 and n_{os} is an oversampling factor (2 is used most generally for this value). Using the critical spacing solved for above I get that our sampling rate is 3.56 arcsec/s. After completing the data collection process I am left with raw data cubes from Green Bank for each session that need to be properly baselined and corrected for receiver error.

2.2 Data Reduction

The first step of the data reduction process was to parse through the raw data and find specific frequencies, feeds, and polarizations that had non-source emissions known as Radio Frequency Interference (RFI). The specific channels of the data that contain this internal interference have been flagged. For example, in our data set AGBT21A_190_01 there are 6 non-source emission spikes within the bandpass. This RFI is shown in Figure 2.1.

The easiest way to flag the appropriate feeds, frequencies, and polarizations is to sum all of the scans taken at a specific frequency, with a specific beam number, and the same polarization. This creates one scan for each which I then iterate through in GBTIDL. This allows me to be able to identify which specific frequencies, beams, and polarizations are having problems. Then I go back to the raw data set and iterate through each raw data scan in that specific frequency, beam number, and polarization to find which scans I have to flag within GBTIDL using the 'flag' method. The RFI could come in the form of an external source or an internal error. External being emission from some unknown source within our bandpass, and internal being internal to the electronics system itself. This means either at the receiver or sometime down through the "back-end" of the receiver I am getting imperfections that are interfering with our data. The specific data interference I see is most likely an internal receiver error. This makes the reduction process much easier because the errors conform to a specific pattern that I am able to flag.

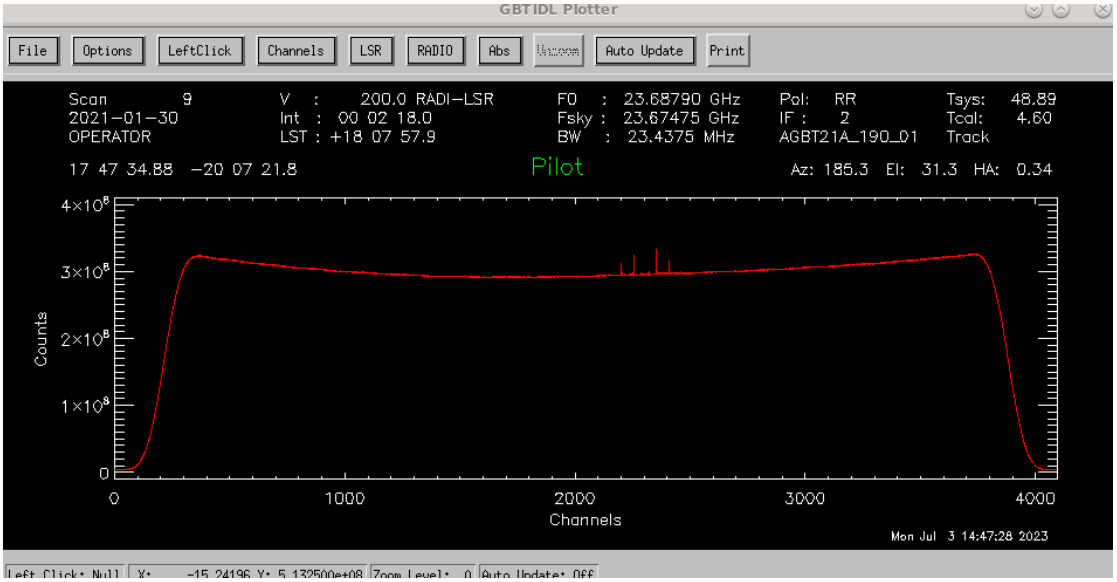

FIGURE 2.1: Example of RFI from frequency 2, feed number 1, and polarization 1. Each of the spikes shown here is around 3 channels wide and there are 6 separate spikes. The pattern shown here is seen in multiple different scans across multiple different frequencies meaning this is most likely internal errors coming from within the receiver.

Once the RFI was removed I was able to begin other reductions such as data smoothing to maximize the signal-to-noise ratio of the emission. This was less important for the bright and obvious NH_3 (1,1) lines which show their hyperfine structure, but it was very important for the NH_3 (4,4) line transition which is much deeper within the noise. Multiple tactics were employed: splitting the raw data cube up into its individual spectra, smoothing the 'off' data set, baselining as effectively as possible, and then regridding the data into a reduced data cube. The data cubes I used from the GBT using the OTF mapping technique have information that needs to be parsed: each scan has a number of integrations, and each one of those integrations is taken at a specific frequency through each of the 7 feed horns, and all of this is done for two polarizations. Using a reduction script with parallel processing capabilities within GBTIDL, I am able to parse through each of these integrations to baseline and smooth the data to lower our RMS noise as much as possible. I smoothed the data by 12 channels which means our final velocity resolution was 0.84 $\mathrm{km\,s^{-1}}$.

Opacity values were also an essential part of the data reduction. The atmosphere is differing levels of opaque at different frequencies. Since I am taking data at 7

different observed frequencies I have to account for the difference in the opacity of the atmosphere. Atmospheric opacity values are taken from three weather centers near Green Bank. I study satellite images to find out which of the three locations most agree with Green Bank's weather at the time of the observations. If all three agree I would use an average. The opacity values were taken every hour on the hour, but I want specific opacity values at the time of each data scan. So I write a script that interpolates the hourly opacity values to the specific scan times found within the raw data. This script also does this for every associated frequency value. These opacity values are merely interpolated estimations, as I do not have specific measurements of the opacity values at every specific scan time. These opacity values are added to a summary file for each specific session of collected data.

Once the reduction script has been run I then regrid the reduced files creating reduced data cubes for each frequency value listed in Table 2.1. Meaning I have obtained a reduced NH_3 (1,1), (2,2), (3,3), and (4,4) cube in fits format for the pilot region. For the edge region I then have a reduced data cube for the NH_3 (1,1) and (2,2) transitions. The cubes are Position-Position-Velocity (PPV) cubes with velocity as the spectral axis. The pilot region NH_3 (1,1) data cube is shown with a select number of channels in Figure 2.2. This figure shows the different velocities that are apparent within the Midpoint gas cloud. High-velocity emission to the south of the main cloud is shown in the top left figure. Then as the velocity decreases that emission dissipates and the main core feature of this cloud shows itself around 200 $\mathrm{km\,s^{-1}}$.

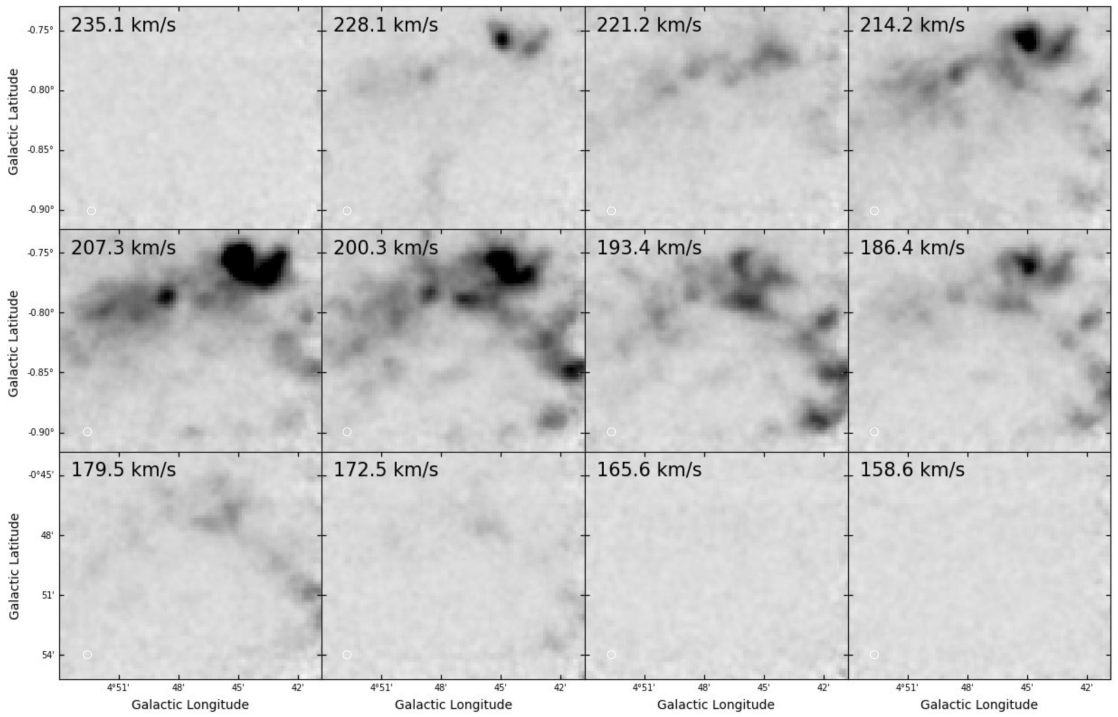

FIGURE 2.2: Selected channel maps of the pilot region of the dust lanes shown in the NH_3 (1,1) emission line. The channel velocity is shown in the top left corner of each panel. These maps have a velocity resolution of 6.95 $\mathrm{km\,s^{-1}}$ in comparison to the actual dataset with a resolution of 0.84 $\mathrm{km\,s^{-1}}$. The data range is -0.15K $\sim$ 0.5K.

CHAPTER 3: Analysis

3.1 Moment Map Analysis

Now that our data has been baselined and cleaned of all internal receiver error I can calculate moment maps 0, 1, 2, and 8 to visualize my 3D data cubes within 2D projections. As we know our 3D data cubes consist of two position dimensions and then a third spectral axis which is a velocity spectrum at each pixel of the cube. These 2D projection moment maps break down the spectrum at every location into a statistical model of the data. An example spectrum is shown in Figure 3.1.

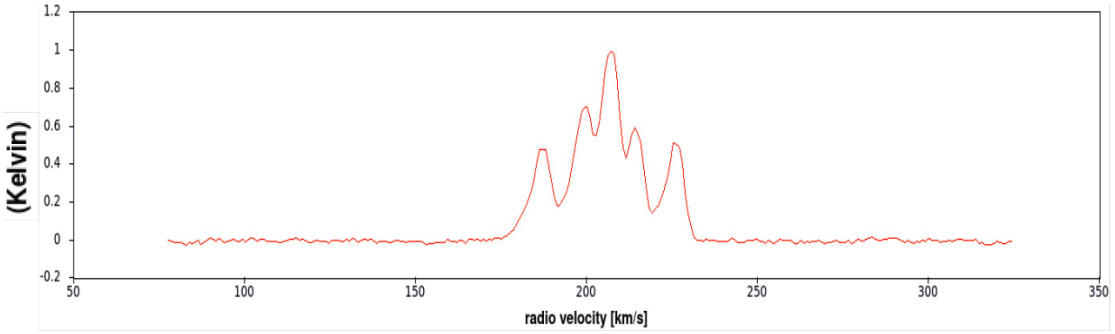

FIGURE 3.1: Example midpoint spectrum of brightest region shown in Figure 3.8.

The first moment map that I calculate is the integrated intensity map. This moment map takes the spectrum that is located at each individual pixel and integrates it over the entire range of velocity values. This map allows a two-dimensional representation that highlights the pixels with the most overall emission across the entire range of velocity values. During the calculations of moment 0, I set a parameter that cuts off the edges of the spectrum. At the edges of the spectral window there are spectral window edge effects that create wavier baselines. Figure 3.1 shows a nicely baselined spectrum, so cutting off the edges of the spectrum will not affect the look of the moment 0 map. However, the spectra that are associated with the edge region contain a slightly wavier baseline. The waviness in the edge region emission is not an extra satellite line of NH_3, but rather a leftover section of a wavy baseline. When doing our analysis in the Common Astronomy Software

Applications (CASA) I have set a range of channels to calculate the moment 0 map between, which will cut off these edge effects. Moment 0 is the integrated intensity of our emission shown in Equation 3.1:

$$M_0 = \int T_A^*(v)dv \tag{3.1}$$

where T_A^* is the temperature or measured emission and ν is the frequency or spectral axis. Figure 3.2 shows the moment 0 maps for each of the NH_3 transitions ((1,1), (2,2), (3,3), and (4,4)) for the pilot region, and Figure 3.3 shows the moment 0 maps for the NH_3 transitions ((1,1), and (2,2)) for the edge region. These maps allow us to see the location of the gas at each transition within the cloud. Figure 3.2 shows that most of the gas is concentrated at around 4.75°, -0.75° gal. There is also a visually distinct region at around 4.80°, -0.87° gal. This region is not as bright as the main branch of the cloud but is interesting to look at when we discuss its velocity components for the moment one map. Looking at the data ranges used within the caption for Figure 3.2 it can also be seen how the integrated intensity differentiates between the four different transitions. The larger data range means a larger overall integrated intensity. The only outlier in terms of the integrated intensity dropping off as we go to higher transitions is the NH_3 (3,3) transition.

Shown in Figure 3.3 there are two main branches of this Edge cloud. One located at around 8°05', -0°27' gal and one located at around 8°0', -0°30' gal. The first region is the brighter region with dimmer emission surrounding both of these regions. From these plots, the regions are connected through the dim gas emission and are therefore not two completely distended globules within physical space (as discussed more with dendrograms later in this chapter). The same trend is also seen here where the NH_3 (1,1) map has a higher range of pixel values than the NH_3 (2,2) map.

Moment one is the weighted average intensity of the spectral axis, as shown in Equation 3.2:

$$M_1 = \frac{\int T_A^*(v)vdv}{\int T_A^*(v)dv}. \tag{3.2}$$

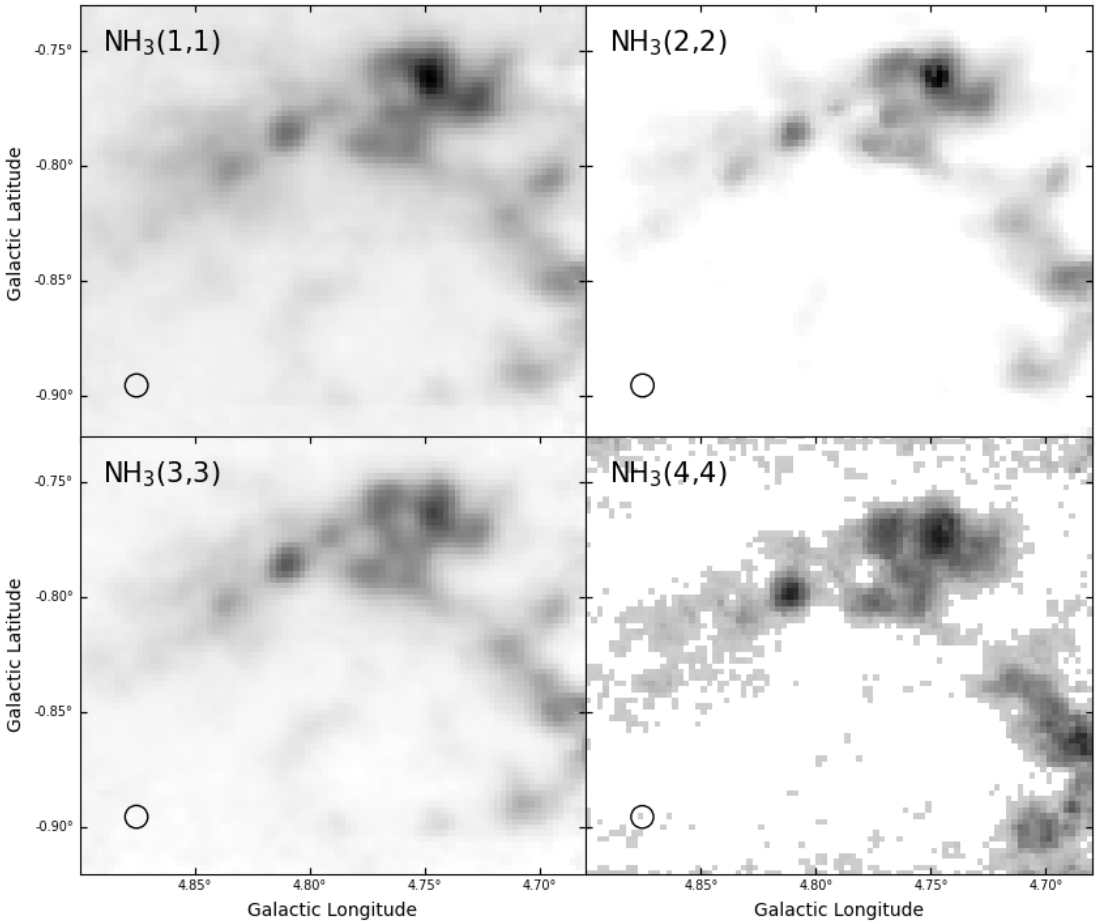

FIGURE 3.2: Midpoint integrated intensity map (Moment 0) from NH_3 gas tracer in the pilot region with specific transition state labeled in the top left corner. The data range for the NH_3 (1,1) map is -2K∼24K, for NH_3 (2,2) it is 0K∼8K, for NH_3 (3,3) it is 0K∼20K, and for NH_3 (4,4) it is -1K∼2.5K.

These moment one maps represent the average velocity values of the spectra at each pixel for each associated data cube. The pilot region moment one maps are displayed in Figure 3.4, and the edge region moment 1 maps are displayed in Figure 3.5. Within Figure 3.4 we see the radial velocities of the pilot region ranging from 190 $\mathrm{km\,s^{-1}}$ to 215 $\mathrm{km\,s^{-1}}$. Here once again we see the same distention from Figure 3.2 shown prominently in red for the NH_3 (1,1), (2,2), and (3,3) transitions. Figure 3.4 also shows the velocities decreasing as we move to smaller galactic longitudes within this cloud. This leads to an interesting discussion about opposite rotation where the cloud has smaller velocity on the side of the cloud that is accreting into the CMZ first. This is the opposite of what one would expect. This opposite rotation will be discussed more in Chapter 4. Within all of the maps in Figure

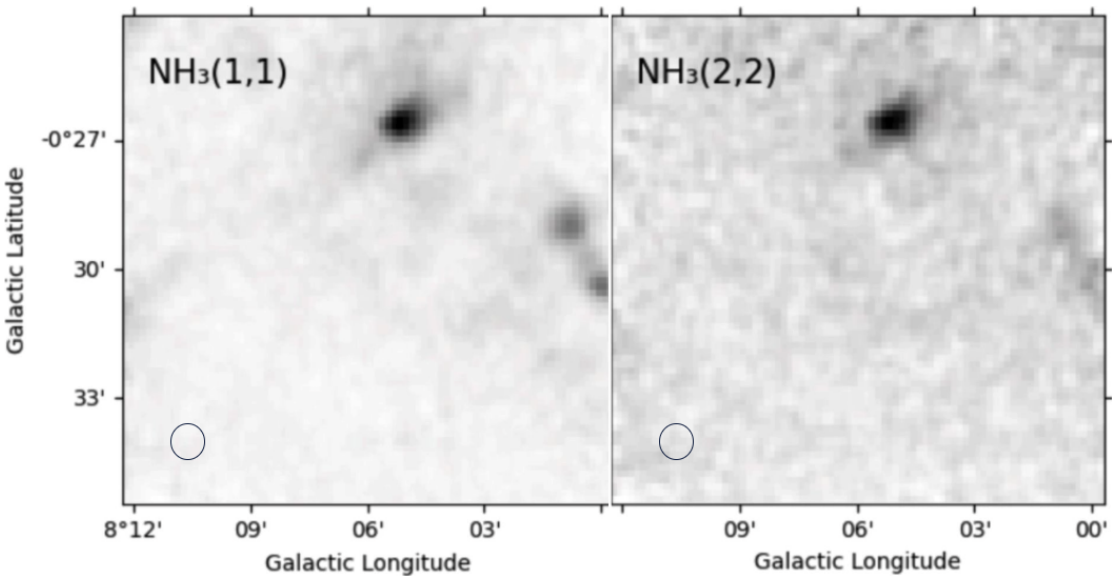

FIGURE 3.3: Midpoint integrated intensity map (Moment 0) from NH_3 gas tracer in the edge region with specific transition state labeled in the top left corner. The data range of the NH_3 (1,1) map is -0.8K∼10K and the NH_3 (2,2) is -0.4K∼1.8K.

3.4 there is a part of the main body of the cloud in the lower galactic latitude area that has a higher velocity that agrees more so with the distended cloud. This would lead to the assumption that these two clouds are connected in some way to rotate together. Another important note is the velocity discontinuity within the NH_3 (3,3) line. This shows up within the branch of the cloud that is not connected. There is the red portion of this emission region which represents the higher velocity component, then within a pixel difference, there is a drop off to the lower velocity limit of this plot. The implication of a velocity discontinuity will also be discussed within Chapter 4.

The edge region is shown within Figure 3.5 and there are lower velocity values when compared with the pilot region. The two moment 1 maps for the edgre region look much worse in comparison with the pilot region due to the fewer number of scans that were taken of the edge region. A similar result is seen within the NH_3 (4,4) line within the pilot region. There also seems to be a rotation going on around the densest region of this cloud (8°05', -0°27' gal) because of the lower velocity region within the middle of the region when compared to the higher or lower velocity values that surround it. The NH_3 (1,1) line also shows the velocity discontinuity

as described for the pilot region moment one map. This is seen when the portion of the cloud lower in galactic latitude goes directly from a higher red velocity value to a lower blue velocity value within the span of one pixel. This will be compared with the pilot region when implications of a velocity discontinuity are discussed in Chapter 4.

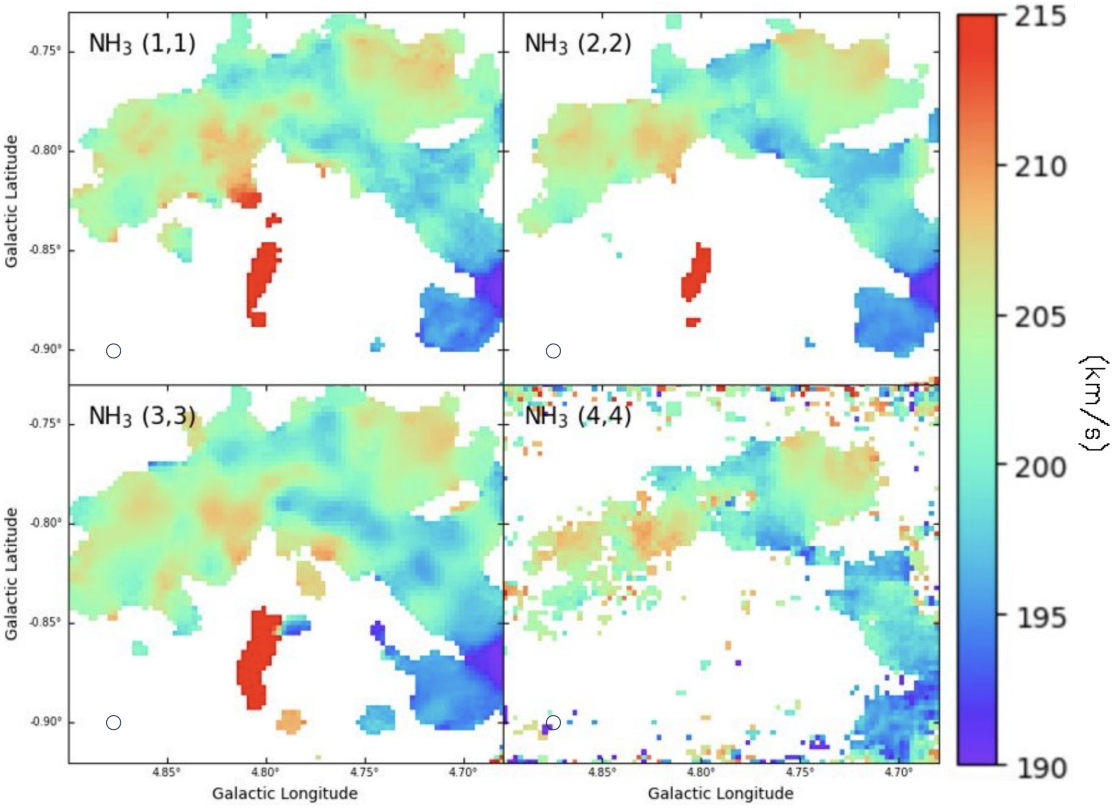

FIGURE 3.4: Midpoint intensity weighted velocity field (Moment 1) from NH_3 gas tracer in the pilot region with specific transition state labeled in the top left corner.

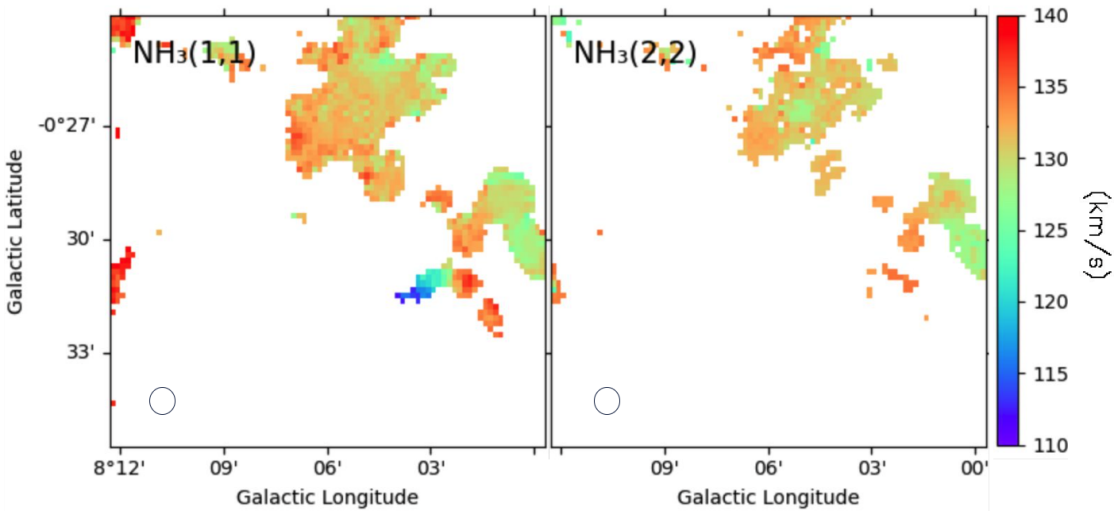

FIGURE 3.5: Midpoint intensity weighted velocity field (Moment 1) from NH_3 gas tracer in the edge region with specific transition state labeled in the top left corner.

Moment 2 is the dispersion of the spectral axis as taken from the full width at half maximum (FWHM), as shown in Equation 3.3:

$$M_2 = \sqrt{\frac{T_A^*(v)(v - M_1)^2 dv}{\int T_A^*(v) dv}}. \tag{3.3}$$

These moment 2 maps represent the full width at half maximum of each spectrum at each pixel location for each data cube. The moment two maps for the pilot region are shown in Figure 3.6 and the moment two maps for the edge region are shown in Figure 3.7. Within Figure 3.6 it is clear that the regions with the densest emission from the moment zero maps (Figure 3.2) correspond to the areas with the highest velocity dispersion. The same distention is shown in these maps. Specifically in the NH_3 (3,3) map there is another velocity discontinuity. This discontinuity is now a region where the velocity dispersion drops from around $10 \mathrm{km\,s^{-1}}$ to $1 \mathrm{km\,s^{-1}}$. The edge region shows a similar structure in terms of the denser regions having the higher velocity dispersion.

Lastly, moment 8 is the maximum value of the spectrum. This map is used to see the brightest value throughout the entire velocity spectrum and, along with moment map 0, is usually the first moment map to look at to get a sense of how the data looks. The moment 8 map in Figure 3.8 shows our maximum emission at

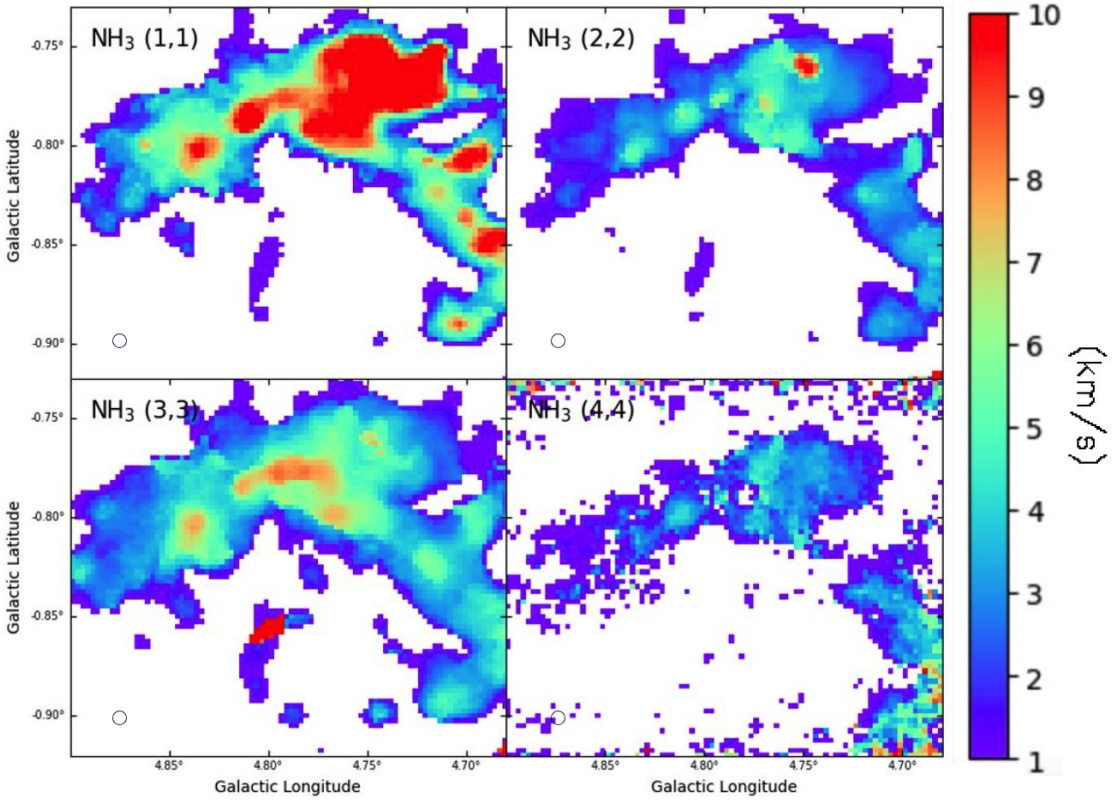

FIGURE 3.6: Midpoint intensity weighted velocity dispersion (Moment 2) from NH_3 gas tracer in the pilot region with specific transition state labeled in the top left corner.

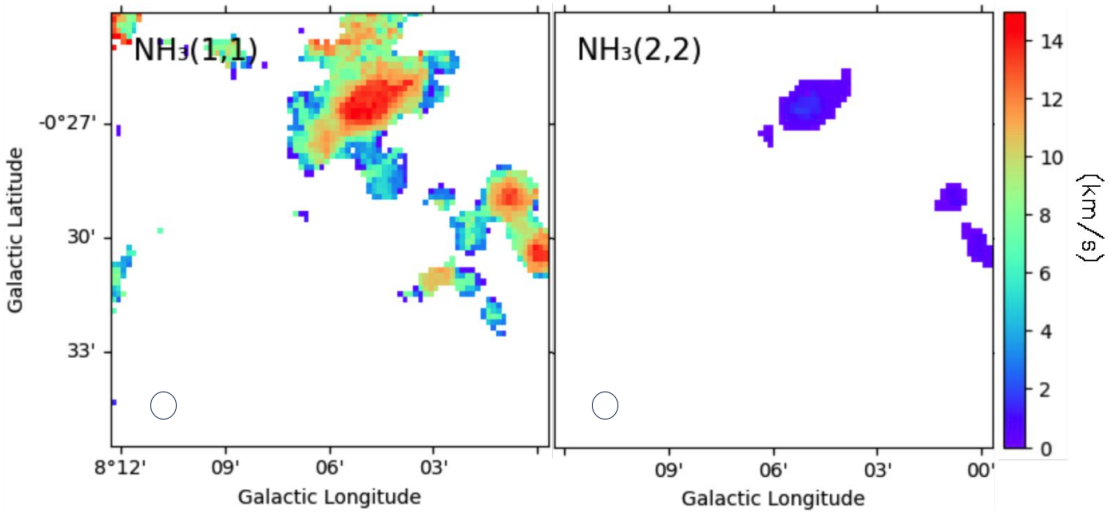

FIGURE 3.7: Midpoint intensity weighted velocity dispersion (Moment 2) from NH_3 gas tracer in the edge region with specific transition state labeled in the top left corner.

every pixel location for the pilot region. This not only shows where the brightest emission along the spectral axis for this transition, but it also more easily shows the weaker, extended emission. The moment 8 map for the edge region is shown in Figure 3.9. The moment 8 map for the pilot region shows some of the same features as seen in the moment 0 maps. The main advantage of the moment 8 map is being able to show the lower emission regions. For example, within Figure 3.8 there is a connecting region between the distended emission (4.80°, -0.87° gal) and the main body of the gas cloud. This connecting emission is not seen as clearly in Figure 3.2.

Within Figure 3.9 the less bright emission in this region shows much more when compared with Figure 3.3. Moreover, there is much less dim emission in the edge region than in the pilot region when comparing Figure 3.9 and Figure 3.8.

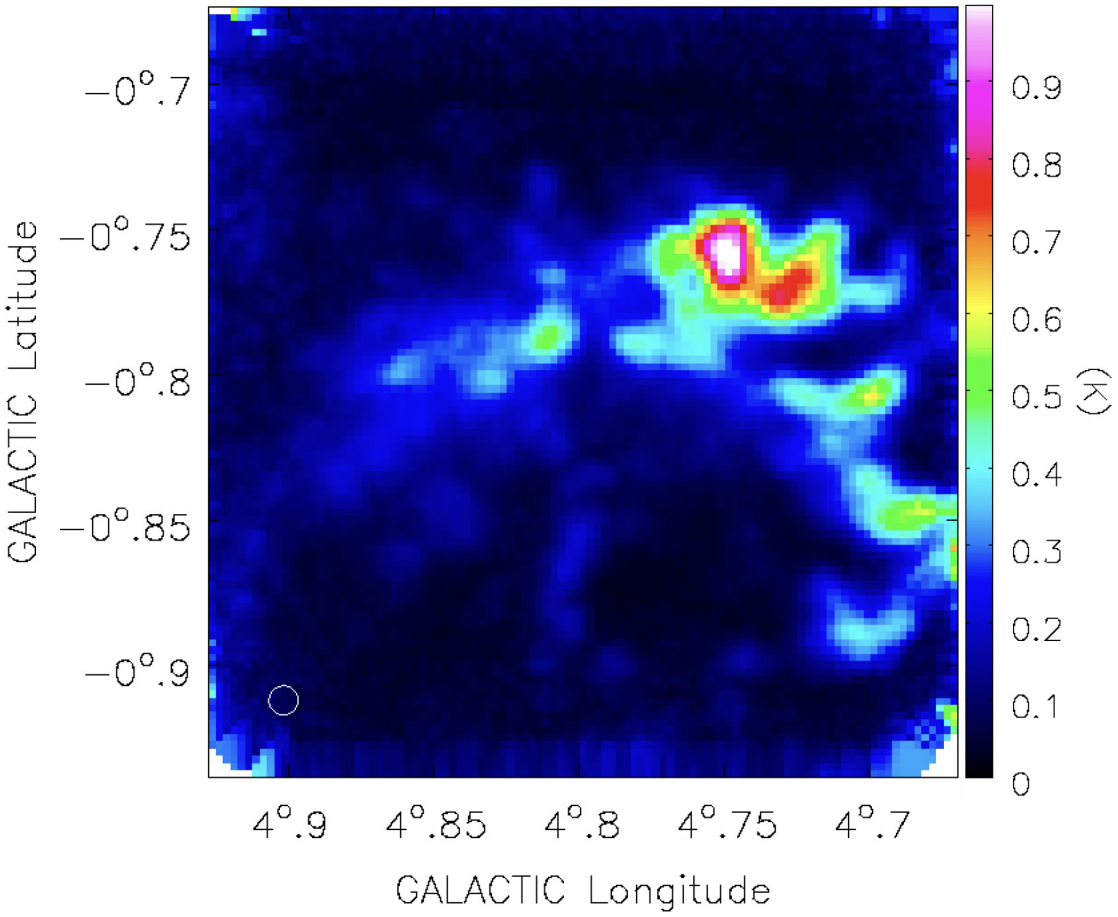

FIGURE 3.8: Midpoint maximum emission value map (Moment 8) from the NH_3 (1,1) gas tracer for the pilot region.

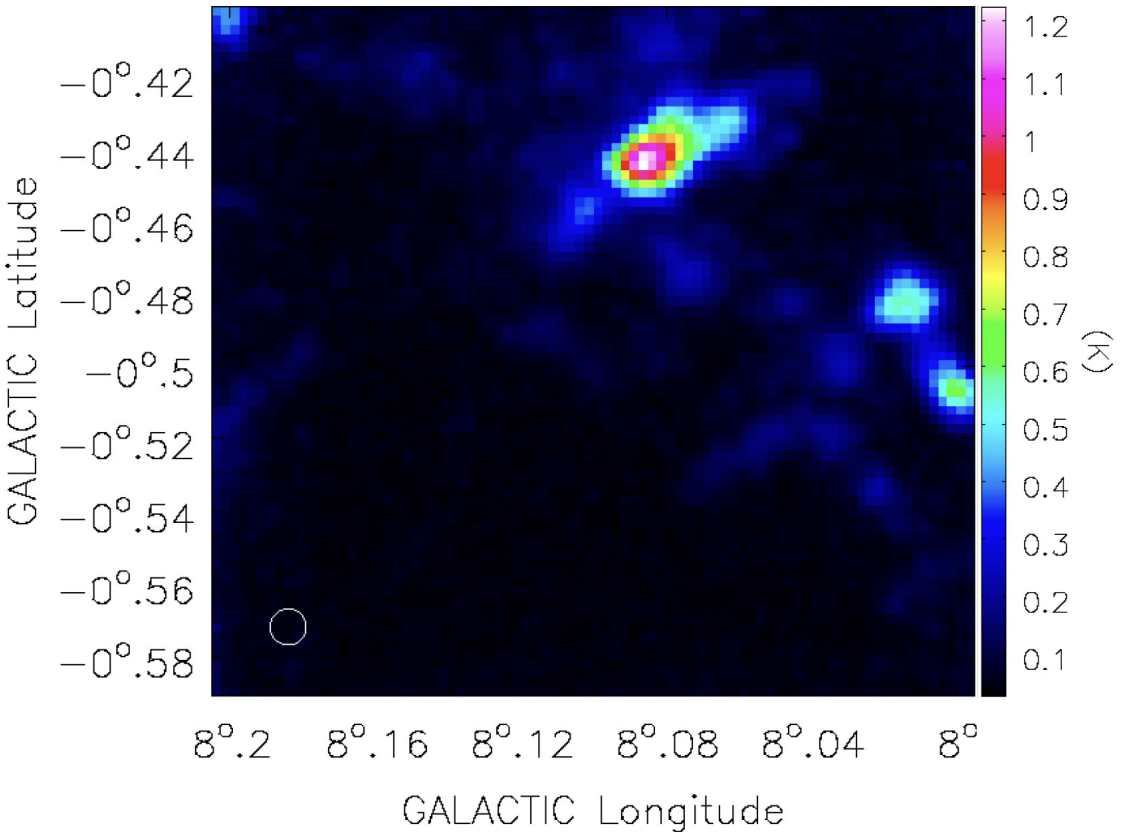

FIGURE 3.9: Midpoint maximum emission value map (Moment 8) from the NH_3 (1,1) gas tracer for the edge region.

From these detections with the moment maps, I now solve for the temperature of the systems by relating two different NH_3 transitions. Column densities are first calculated for each transition. Keep in mind for our calculations I am only using metastable NH_3 transitions, meaning J=K for the quantum numbers. Now I solve for the column densities from Mauersberger et al. (2003):

$$N(J,K) = \frac{1.55 * 10^{14} cm^{-2}}{\nu} \frac{J(J+1)}{K^2} M_0. \tag{3.4}$$

In Equation 3.4, J and K are the quantum numbers, ν is the line frequency in GHz, and M_0 is the moment zero value in K km s^{-1} at every pixel location. So from this equation, I am able to solve for an array of beam-averaged column densities for this rotational state of NH_3 at each pixel. The output of the pilot region column density maps is shown in Figure 3.10 for NH_3 (1,1), Figure 3.11 for NH_3 (2,2), Figure 3.12 for NH_3 (3,3), and Figure 3.13 for the NH_3 (4,4) transition. The edge

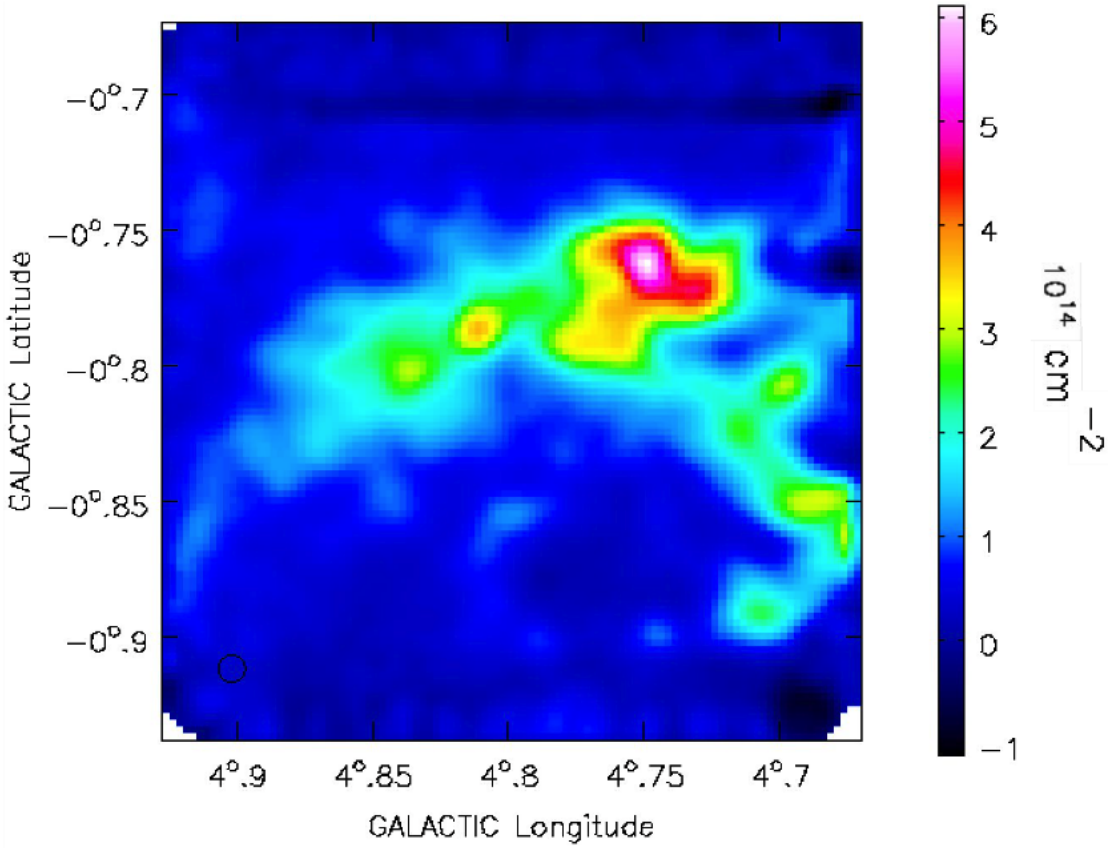

FIGURE 3.10: Column Density map for the pilot region using the NH_3 (1,1) transition. The image map was created using Equation 3.4.

region maps are shown in Figure 3.14 for NH_3 (1,1), and Figure 3.15 for the NH_3 (2,2) transition.

Using the CASA methods imsmooth and reproject I am then able to solve for the temperatures using two different transitions (Equation 3.5). I must use 'imsmooth' and 'reproject' because the beam size of each of our individual transitions is different. The higher the frequency the finer the beam, so I must smooth the finer beam to the wider beam's pixel size. Then I must reproject the smoothed pixels to match up, giving us two data sets with identical pixel size and gridding. Equation 3.5 is then used with the two different transitions:

$$\frac{N_u(J',J')}{N_u(J,J)} = \frac{g_{op}(J')}{g_{op}(J)} \frac{2J'+1}{2J+1} exp(\frac{-\Delta E}{T_{JJ'}}) \tag{3.5}$$

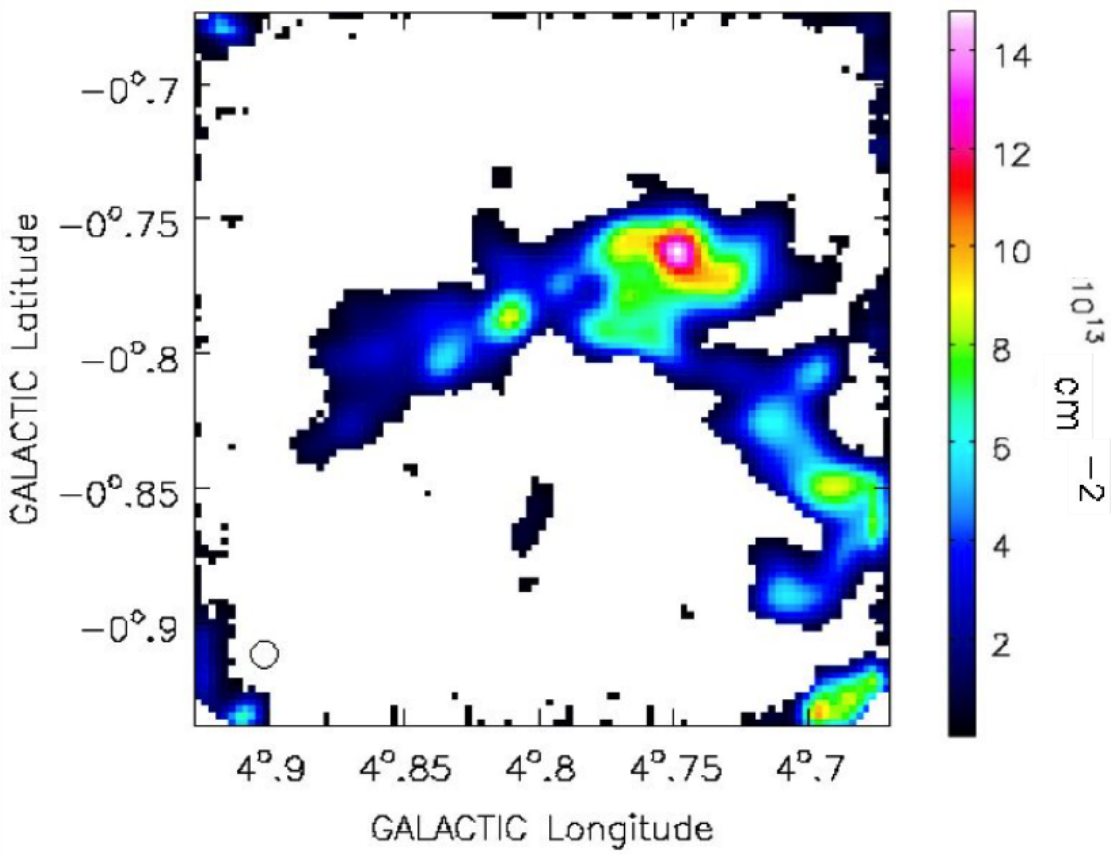

FIGURE 3.11: Column Density map for the pilot region using the NH_3 (2,2) transition. The image map was created using Equation 3.4.

where g_{op} is 1 for para-ammonia, meaning quantum number K=1,2,4,5,7... and is 2 for ortho-ammonia, meaning K=3,6,9..., ΔE is the energy level difference between the two transition lines, and $T_{JJ'}$ is the rotational temperature that I am solving for. For my purposes, I related the (1,1) and (2,2) transitions together to give us a "cold" temperature map for each gas cloud that is being studied. This product is shown in Figure 3.16 for the pilot region, and in Figure 3.18 for the edge region. The contours in Figure 3.16 are taken from the NH_3 (1,1) moment 8 map. Looking at Figure 3.16 it can be seen that the temperature values range between 11K and 23K. The main branch of the cloud shows hotter cores that are internally heating the colder outer layer of gas. The denser regions as seen in Figure 3.2 seem to correlate to the hotter regions within this gas cloud. For the edge region in Figure 3.18, the data is more difficult to parse. When looking at this map it is important to focus on the regions that have the NH_3 (1,1) moment 0 map contours over them. These regions are more likely to contain physical emission rather than

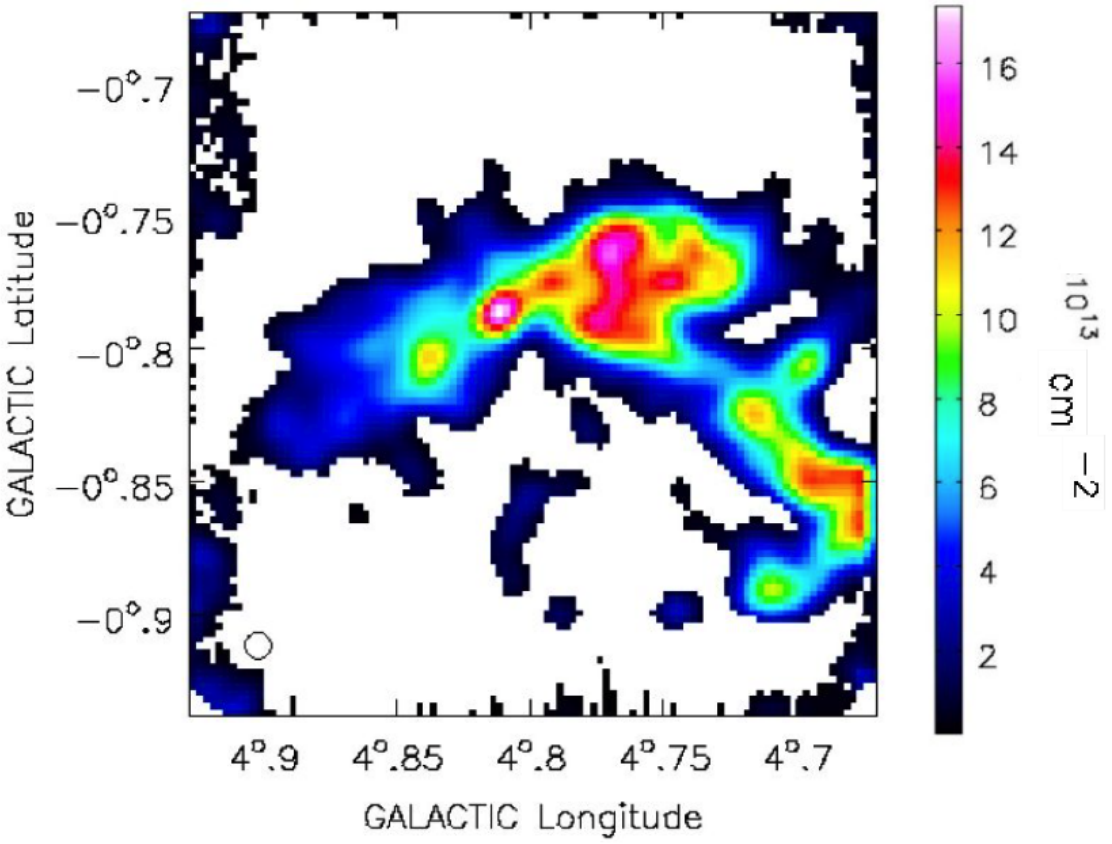

FIGURE 3.12: Column Density map for the pilot region using the NH_3 (3,3) transition. The image map was created using Equation 3.4.

the calculation of the temperature map picking up residual noise. When looking at these contours we see similar qualities as the pilot region. The central clump of this cloud (8.08°, -0.44°gal) shows relatively warmer regions towards the center, other than the section of this cloud that is bright red on the edge of the moment 8 contour line. The lower emission region adjacent to the main clump shows up just as cool as the less bright emission regions.

In the next temperature map, I have related the (2,2) to the (4,4) transition giving us the "warm" temperature map for the pilot region. This map was only done for the pilot region because the edge region did not have data taken in the NH_3 (4,4) transition. This warm map is shown in Figure 3.17. This figure has the same NH_3 (1,1) moment 0 emission map contours as the cold temperature map. This map shows a similar structure to the cold temperature map, where the hotter emission is located towards the central regions of the gas cloud. This shows an internally

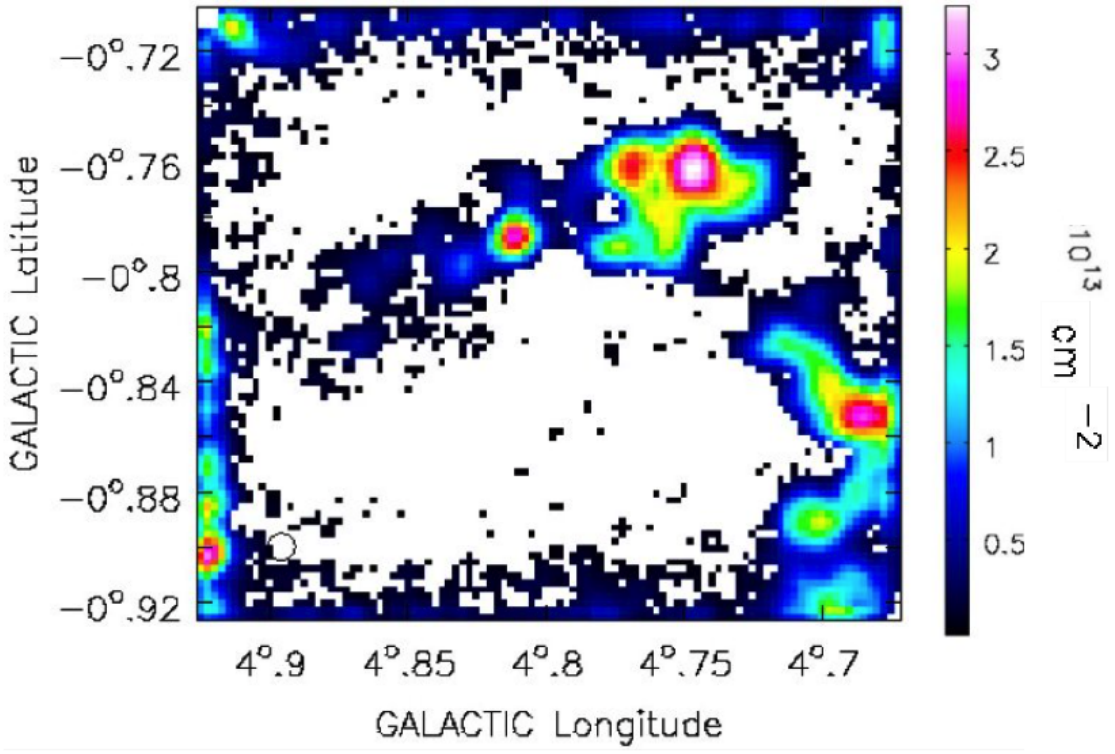

FIGURE 3.13: Coolumn Density map for the pilot region using the NH_3 (4,4) transition. The image map was created using Equation 3.4.

heated core surrounded by colder emission towards the more edge regions of the cloud. The hotter cores of this cloud peak at $\sim$ 90K and the colder outer regions are at $\sim$ 35K. Different ratios, such as the (1,1) to the (4,4) can be taken, but the signal-to-noise ratio drops off as you move to these higher energy transitions. This means comparing the (1,1) to the (4,4) will mostly be tracking the hotter, more dense cores of the gas cloud. So in the literature, most ratios are taken between energetic neighbors such as the (1,1) to the (2,2), and the (2,2) to the (4,4).

3.2 Dendrograms

Dendrogram analysis is used to compare the hierarchical structure of an object or data set. More specifically it is used to visualize hierarchical clustering. The dendrogram structure is completely characterized by local maxima within the dataset provided. These structures can be determined in both 2D (position-position) and

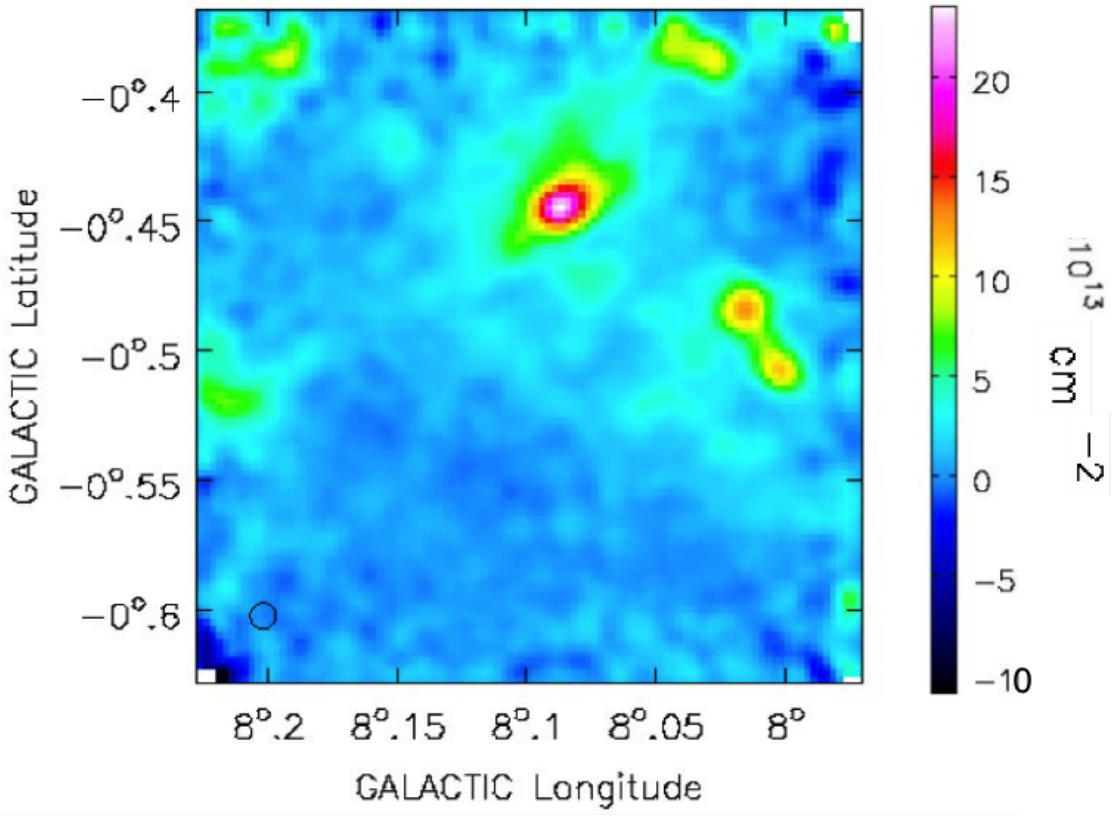

FIGURE 3.14: Column Density map for the edge region using the NH_3 (1,1) transition. The image map was created using Equation 3.4.

3D (position-position-velocity) space. The structures within the dendrogram consist of leaves that come together to make branches and branches that come together to make roots. The highest local maximum of our spectrum is a leaf and as you move down the spectrum more local maxima come together to create new leaves. These new leaves connect to make branches. We also give parameters to the Astrodendro code so that noise products that contain local maxima are not counted as leaf structures. An example of an emission spectrum and corresponding dendrogram plot is shown in Figure 3.19. This strategy was applied by Rosolowsky et al. (2008) which analyzed ^{13}CO (J = 1 $\longrightarrow$ 0) data from the L1448 region in Perseus. Originally dendrograms were designated as 'structural trees' allowing the characterization of hierarchical structure by Houlahan & Scalo (1992).

With a basis for what Astrodendro can accomplish I then begin looking at the midpoint of the Milky Way dust lanes using dendrograms. Using a molecular line data cube we have the ability to take advantage of dendrogram analysis and

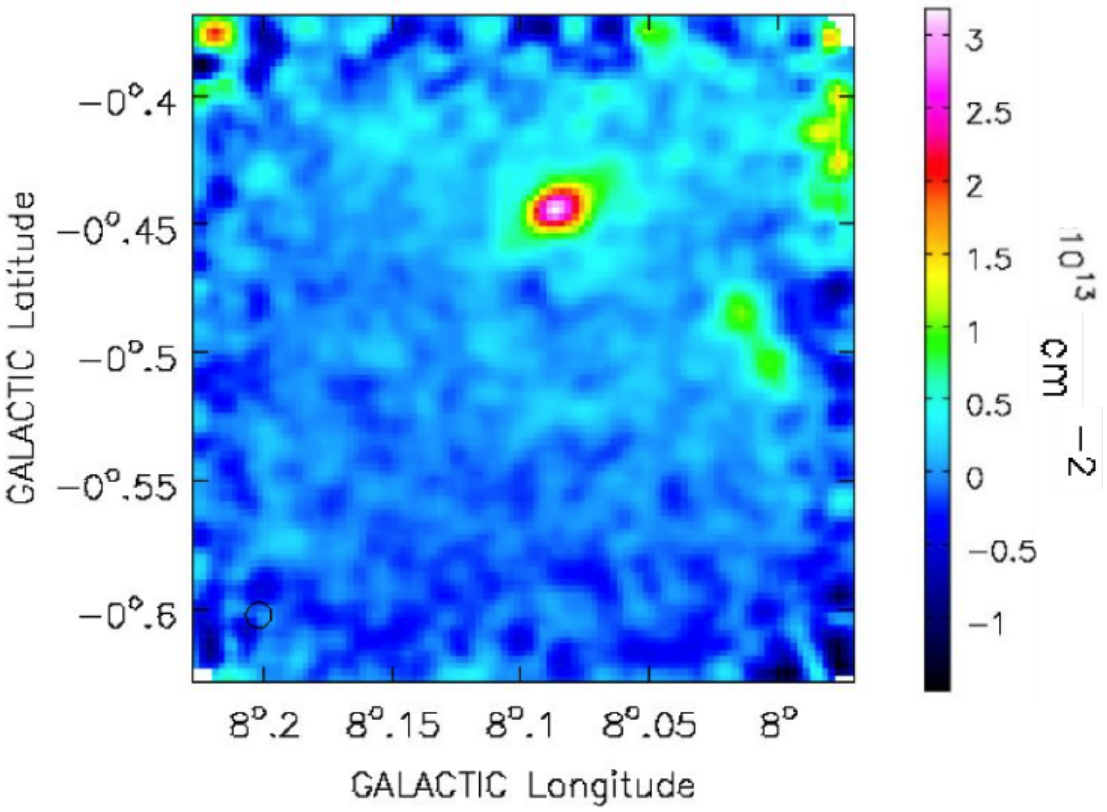

FIGURE 3.15: Column Density map for the edge region using the NH_3 (2,2) transition. The image map was created using Equation 3.4.

analyze hierarchical structure over multiple scales in position and velocity space. This will show within the two gas clouds how each pixel is related through 'roots', 'branches', and 'leaves' as defined by the Astrodendro program. For the pilot region, the dendrogram map is shown in Figure 3.20, with the associated structure hierarchy map shown in Figure 3.21, and the statistics of each structure shown in Table 3.1 and Table 3.2. The colors of the structures match up. For example, within Figure 3.20 the most broadly covered structure is displayed in blue. Within Figure 3.21 the lowest and therefore most expansive trunk is labeled in blue to match. The blue structure itself has many branches and leaves associated with it. These regions are labeled in yellow, green, red, and pink and they represent associated leaves and branches of the main trunk of the system. The red region is a branch of the blue region with an associated leaf labeled in pink. Now taking a look at Table 3.1 and Table 3.2 we can identify statistics associated with structures created by the astrodendro program for the pilot region. When looking specifically at Table 3.2 there are 4 structures (idx 2, 9, 11, and 18) that all share essentially

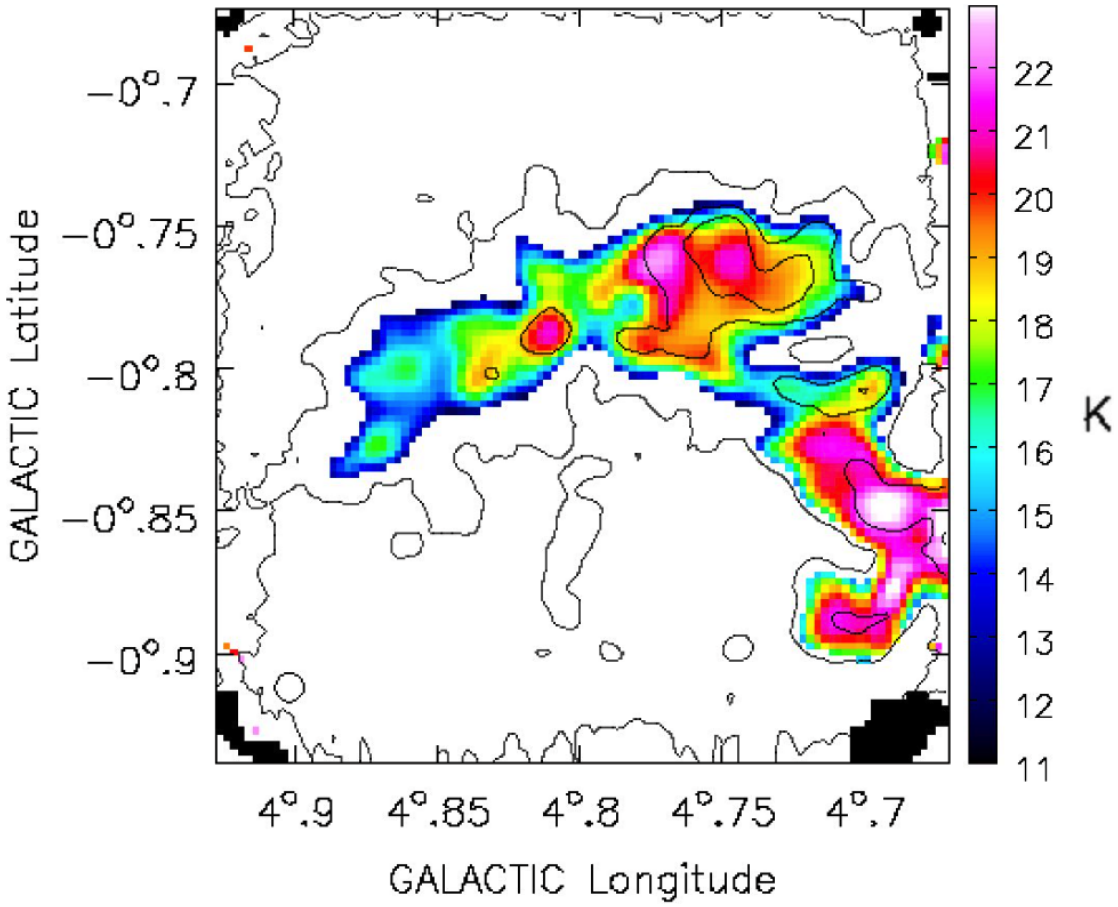

FIGURE 3.16: Cold temperature map for the pilot region using the NH_3 (1,1) and (2,2) transitions. The black contours are 3σ, 9σ, and 14σ detections using the NH_3 (1,1) moment 8 map. I find errors for this temperature calculation to be $\pm$ 6.6K.

the same location on the sky but have wildly varying v_{cen} values. This v_{cen} value is the central velocity of the structure as processed from the data cube through the astrodendro program.

This same process is done with the edge region and shown within the map in Figure 3.22 and the structures within Figure 3.23. We can see from an initial comparison that the edge region structure is much less complex than the pilot region. There are relatively few branches that share a hierarchical structure with associated leaves and branches. There are three main structures within Figure 3.22. The green and yellow regions that show up on the right of Figure 3.22 show up as connected systems within Figure 3.23. The yellow structure therefore shows itself to be consistent with the green structure in a velocity/spatial hierarchy.

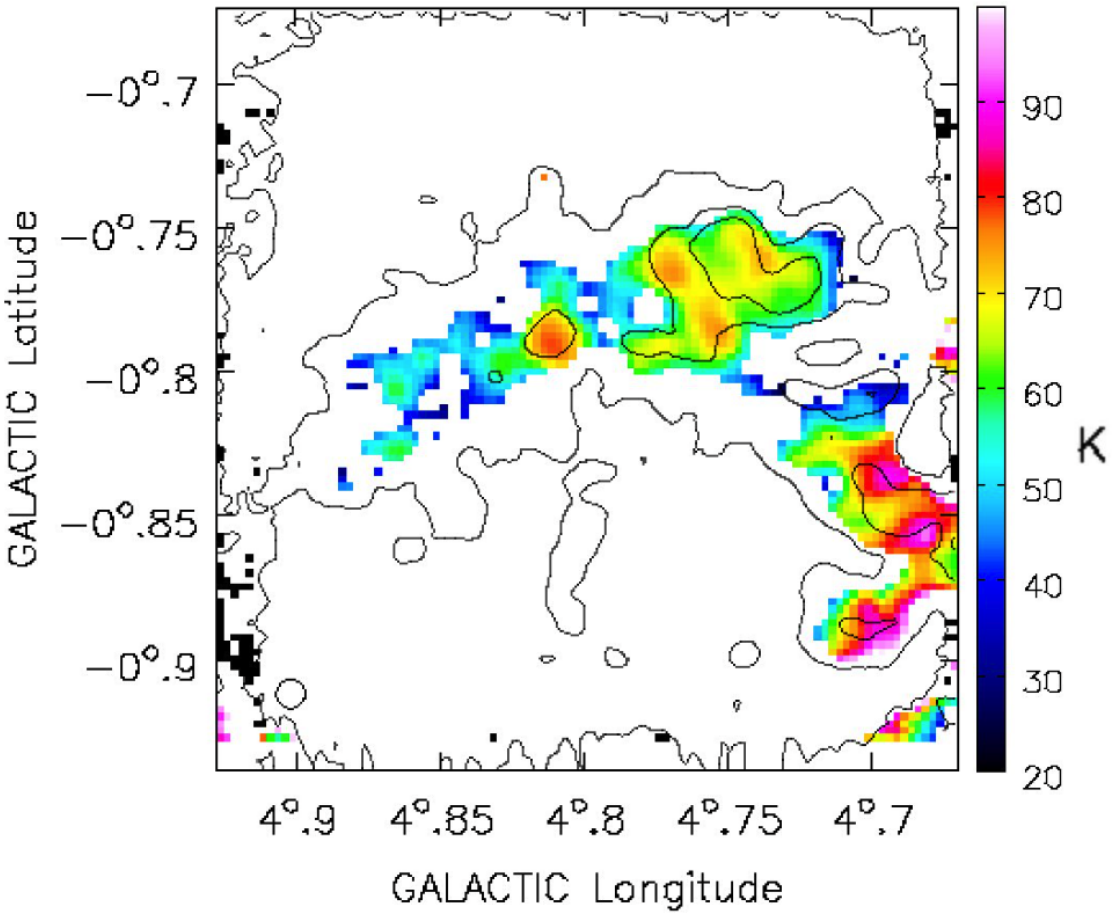

FIGURE 3.17: Warm temperature map for the pilot region using the NH_3 (2,2) and (4,4) transitions. The black contours are 3σ, 9σ, and 14σ detections using the NH_3 (1,1) moment 8 map. I find errors for this temperature calculation to be $\pm$ 3.15K.

Also interesting is the fact that the blue and red structures show up as completely separate structures despite their spatial coherence (also shown within Table 3.4). The meaning of this spatial coherence contrasted with a velocity difference will be explained in Chapter 4.

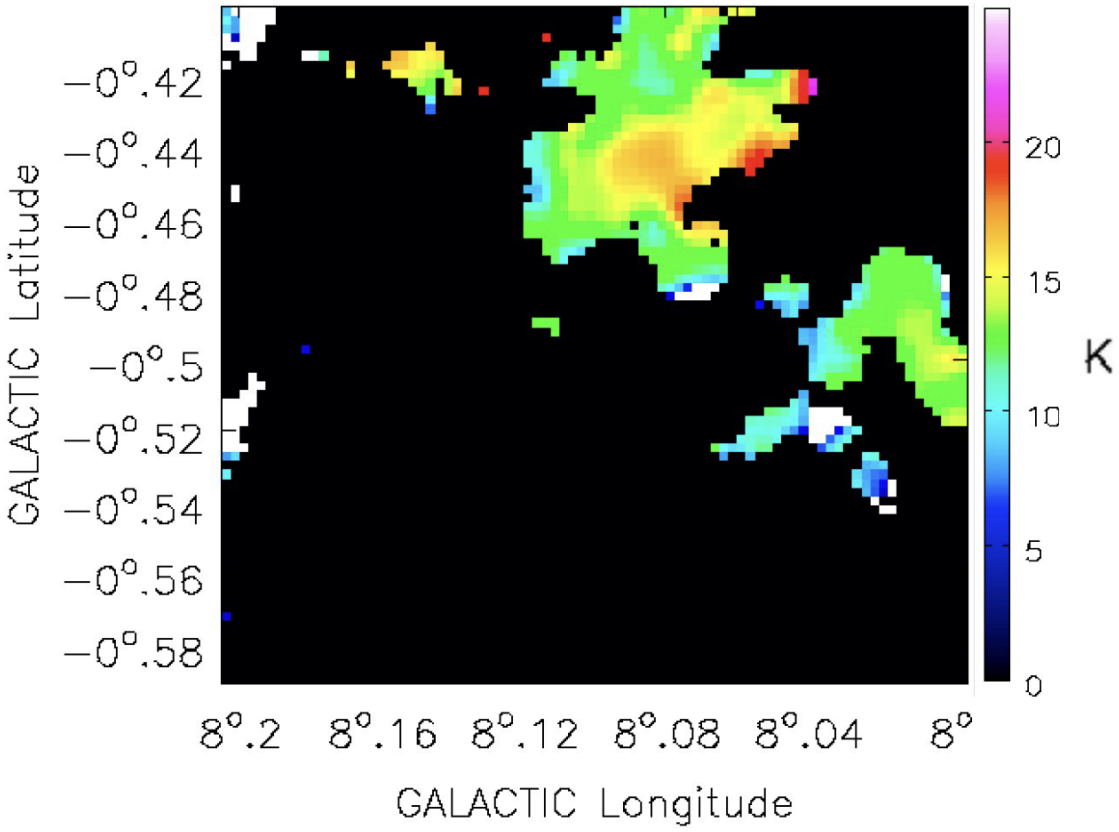

FIGURE 3.18: Cold temperature map for the edge region using the NH_3 (1,1) and (2,2) transitions. The blacked-out region represents those values below a 3σ detection using the NH_3 (1,1) moment 8 map. I find errors for this temperature calculation to be ± 6.6K.

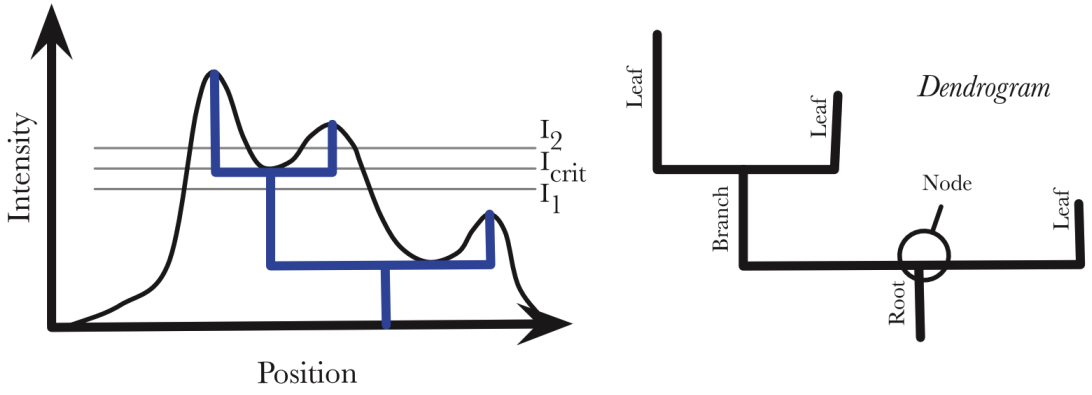

FIGURE 3.19: Dendrogram explanation from Rosolowsky et al. (2008). The left panel shows emission with three local maxima that are noted by the leaves of the dendrogram (as shown on the right). From this dendrogram tree, we see three distinct contour levels. If you threshold at I_1 you see one distinct object and thresholding at I_2 produces two.

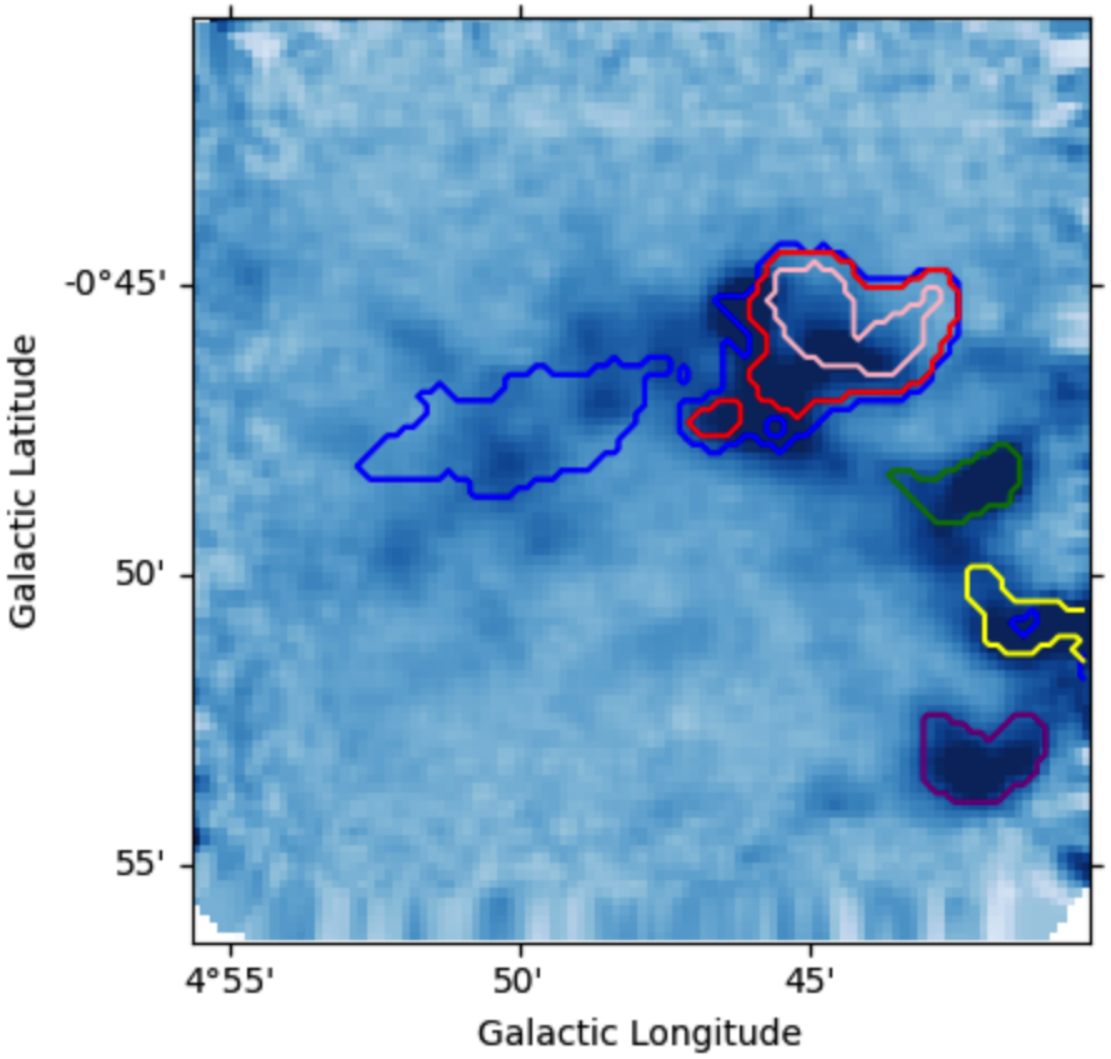

FIGURE 3.20: Dendrogram Map of the pilot region created using Astrodendro package. Each structure with an associated parent structure is shown in the hierarchy in Figure 3.21.

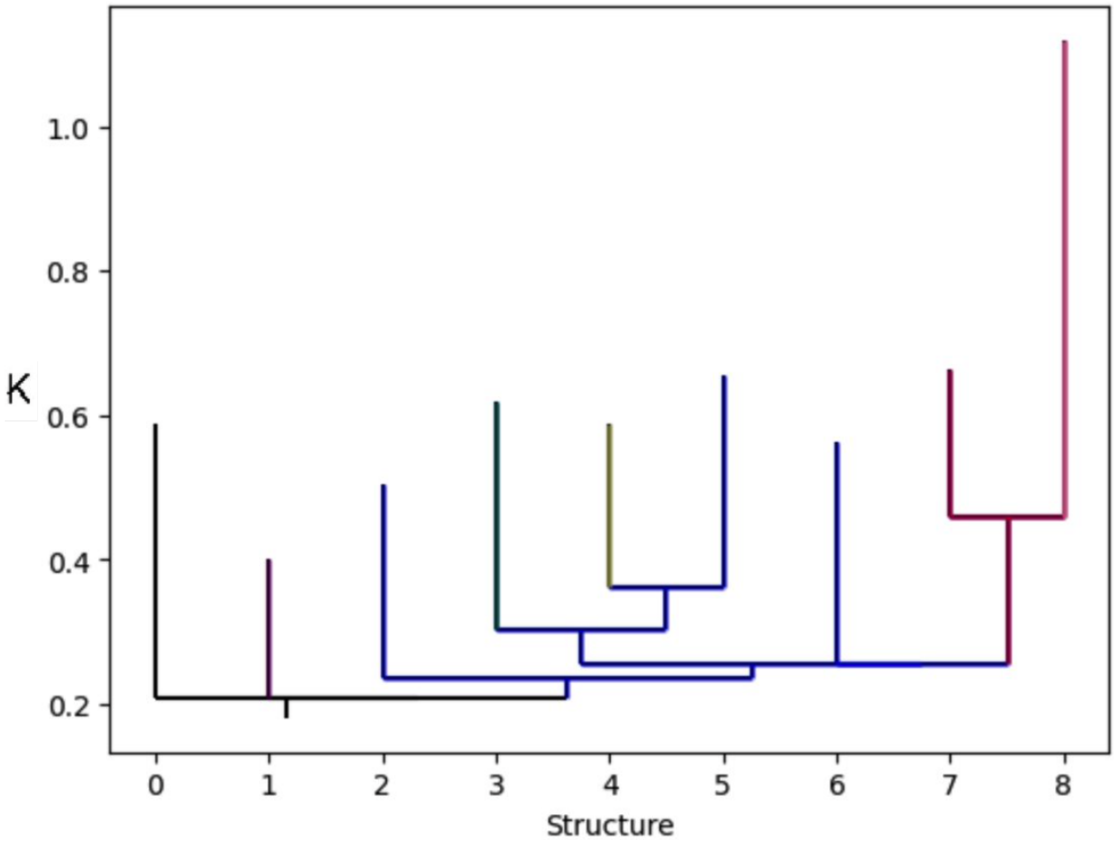

FIGURE 3.21: Dendrogram structure hierarchy plot of the pilot region. Each structure is shown within the dendrogram map in Figure 3.20 and the visual explanation for how each structure is created is shown in Figure 3.19.

TABLE 3.1: Half of the available structure properties of the pilot region. These values were found through the processing of the NH_3 (1,1) velocity cube through the astrodendro program to compute position-position-velocity statistics.

idx	area ellipse arcsec^2	area exact arcsec^2	flux Jy	major sigma arcsec	minor sigma arcsec	position angle deg	radius arcsec
2	4487.36	16200.00	9.57	42.63	24.17	160.65	32.10
5	7863.15	28188.00	26.58	69.25	26.07	-155.88	42.49
9	767.71	2916.00	2.05	15.43	11.43	119.22	13.28
10	604.92	1539.00	0.25	15.13	9.18	-164.54	11.79
11	4732.50	19521.00	34.82	46.02	23.61	159.25	32.96
13	2542.83	10368.00	8.43	30.59	19.09	-168.26	24.16
15	2048.74	7128.00	6.39	30.05	15.65	171.07	21.69
16	2861.23	8424.00	4.49	39.95	16.44	-174.75	25.63
17	433.11	1782.00	1.60	18.80	5.29	90.14	9.97
18	3636.96	12312.00	6.27	45.22	18.47	160.67	28.90
19	255.24	1053.00	0.30	13.61	4.31	91.03	7.66
20	463.88	1539.00	0.27	16.74	6.36	155.00	10.32
21	1397.20	4617.00	0.65	23.57	13.61	-149.28	17.91

TABLE 3.2: The rest of the available dendrogram structure properties of the pilot region. These values were found through the processing of the NH_3 (1,1) velocity cube through the astrodendro program to compute position-position-velocity statistics.

idx	v_{cen}	l	b	axis ratio	radius (from area)
	$\mathrm{km\,s^{-1}}$	deg	deg		arcsec
2	225.16	4.74	-0.76	0.57	71.81
5	205.74	4.82	-0.79	0.38	94.72
9	214.50	4.75	-0.76	0.74	30.47
10	212.72	4.92	-0.68	0.61	22.13
11	204.36	4.74	-0.76	0.51	78.83
13	195.35	4.70	-0.89	0.62	57.45
15	197.24	4.69	-0.85	0.52	47.63
16	195.96	4.71	-0.81	0.41	51.78
17	186.35	4.67	-0.86	0.28	23.82
18	187.08	4.75	-0.76	0.41	62.60
19	166.36	4.67	-0.86	0.32	18.31
20	168.37	4.92	-0.68	0.38	22.13
21	122.43	4.69	-0.93	0.58	38.34

TABLE 3.3: Half of the available structure properties of the edge region. These values were found through the processing of the NH_3 (1,1) velocity cube through the astrodendro program to compute position-position-velocity statistics.

idx	area ellipse	area exact	flux	major sigma	minor sigma	position angle	radius
	$\mathrm{arcsec^2}$	$\mathrm{arcsec^2}$	Jy	arcsec	arcsec	deg	arcsec
0	359.32	1296.00	0.67	11.91	6.93	102.36	9.08
1	453.65	1620.00	0.86	11.86	8.78	97.04	10.21
2	1040.89	4212.00	1.10	19.15	12.48	-153.70	15.46
4	4448.18	14742.00	6.46	36.46	28.01	-146.60	31.96
5	820.90	2592.00	0.72	15.17	12.42	-142.70	13.73
6	1527.14	5508.00	1.36	25.91	13.53	-156.45	18.73
7	3802.73	16443.00	6.63	46.15	18.92	-147.79	29.55
8	2704.97	9315.00	2.60	34.69	17.91	153.44	24.92
9	1121.18	4455.00	1.89	16.47	15.63	-152.07	16.04
11	1124.58	3159.00	0.49	23.84	10.83	70.47	16.07
12	985.53	3807.00	1.21	19.82	11.42	127.78	15.04
13	920.80	3240.00	0.98	22.49	9.40	104.76	14.54
14	1427.42	5589.00	1.59	25.40	12.91	-154.70	18.10
15	1083.22	3969.00	0.80	19.25	12.92	-148.83	15.77
16	577.76	2025.00	0.59	18.74	7.08	108.26	11.52
17	1189.86	3321.00	0.62	24.59	11.11	110.72	16.53
18	493.37	1620.00	0.70	11.94	9.49	94.21	10.64

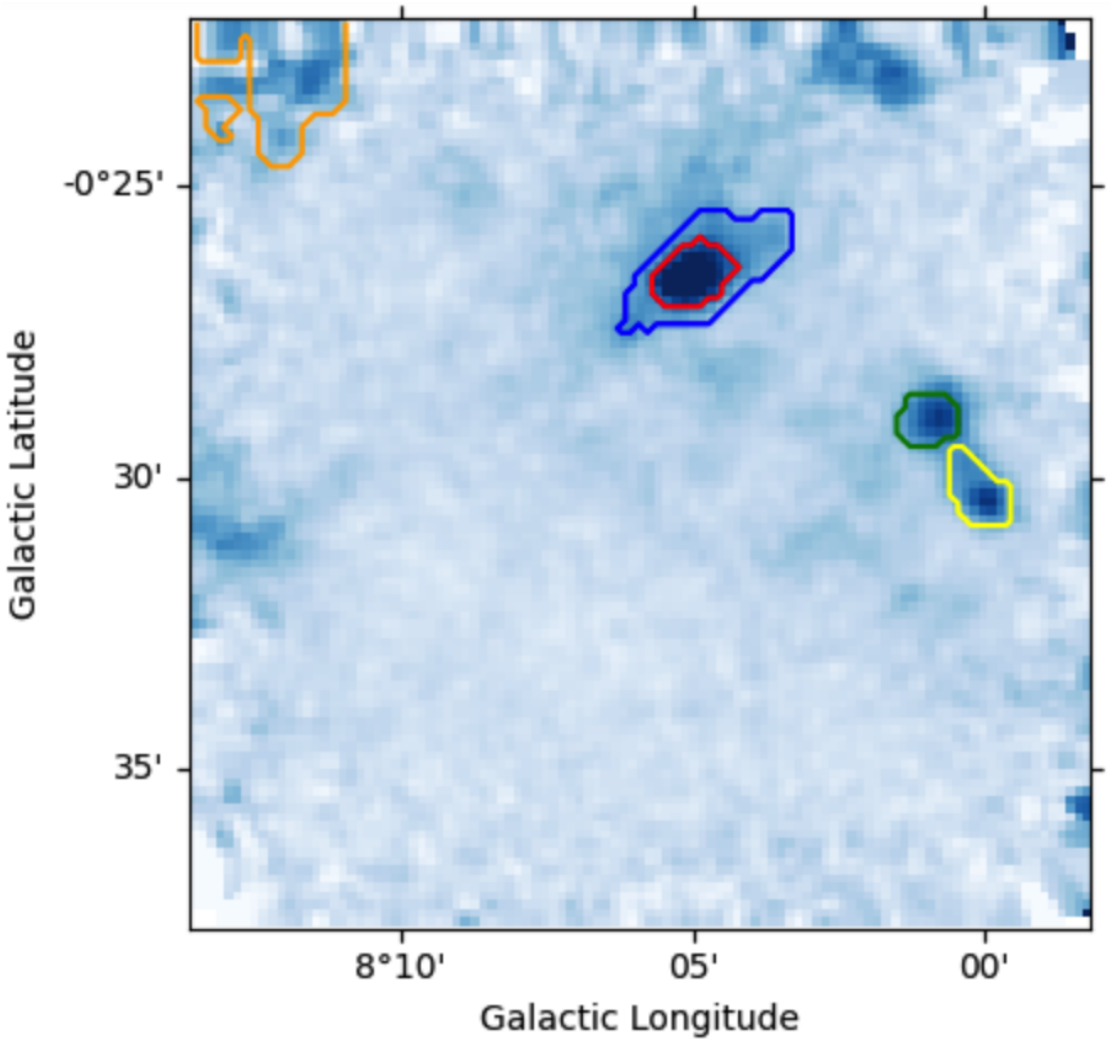

FIGURE 3.22: Dendrogram Map of the edge region created using Astrodendro package. Each structure with an associated parent structure is shown in the hierarchy in Figure 3.23.

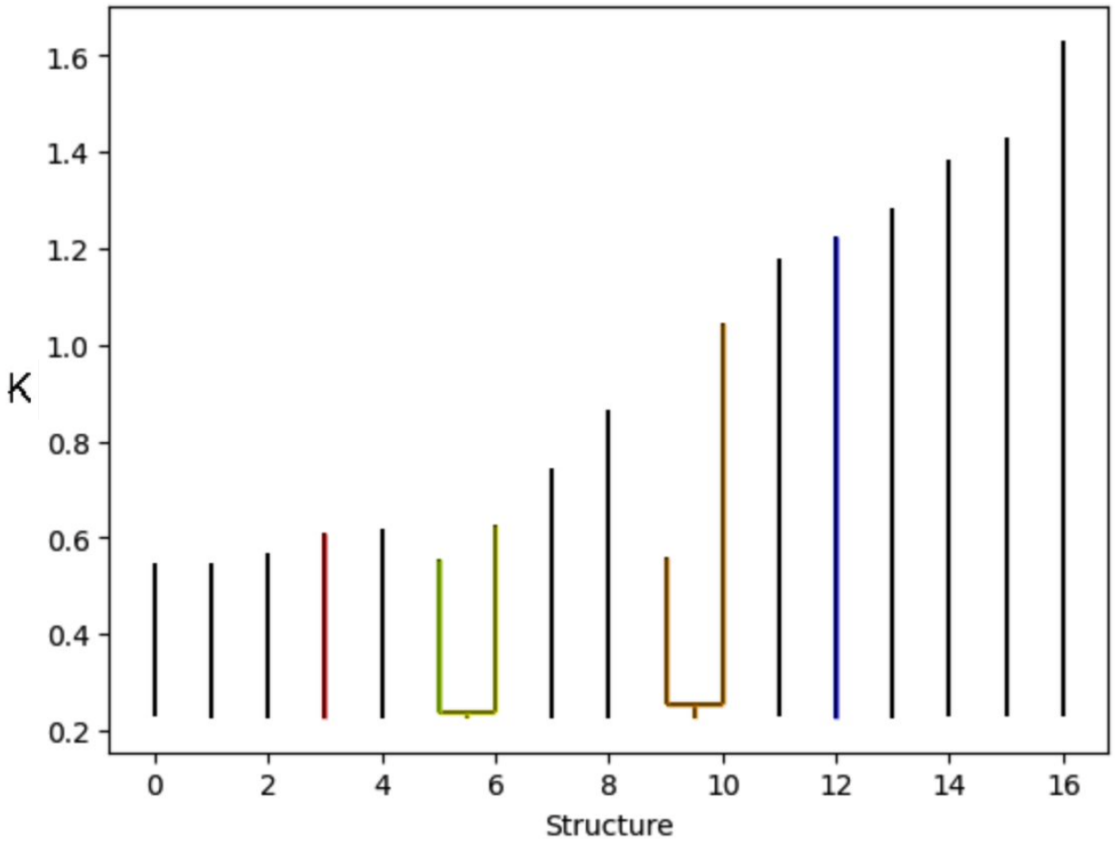

FIGURE 3.23: Dendrogram structure hierarchy plot of the edge region. Each structure is shown within the dendrogram map in Figure 3.22 and the visual explanation for how each structure is created is shown in Figure 3.19.

TABLE 3.4: Half of the available structure properties of the edge region. These values were found through the processing of the NH_3 (1,1) velocity cube through the astrodendro program to compute position-position-velocity statistics.

idx	v_{cen}	l	b	axis ratio	radius (from area)
	$\mathrm{km\,s^{-1}}$	deg	deg		arcsec
0	174.73	7.98	-0.37	0.58	20.31
1	160.13	7.98	-0.37	0.74	22.71
2	150.45	8.08	-0.44	0.65	36.62
4	141.43	8.20	-0.38	0.77	68.50
5	140.16	8.22	-0.37	0.82	28.72
6	138.60	8.08	-0.44	0.52	41.87
7	131.05	8.08	-0.44	0.41	72.35
8	132.02	8.03	-0.38	0.52	54.45
9	130.19	8.01	-0.48	0.95	37.66
11	128.71	8.22	-0.38	0.45	31.71
12	127.76	8.00	-0.51	0.58	34.81
13	127.44	7.98	-0.38	0.42	32.11
14	123.37	8.08	-0.44	0.51	42.18
15	111.53	8.08	-0.44	0.67	35.54
16	111.75	7.98	-0.38	0.38	25.39
17	76.19	7.98	-0.38	0.45	32.51
18	72.10	7.98	-0.37	0.79	22.71

CHAPTER 4: Discussion

4.1 Pilot Region

After doing some analysis with our fully cleaned data I probe the velocity values of each of the clouds using the moment maps created in Chapter 3. We can see from Figure 3.4 that the velocity of the gas cloud within the pilot region is around ∼205 $\mathrm{km\,s^{-1}}$. We can observe from Figure 1.2 (red box) that this velocity is consistent with the expected velocity of this gas cloud as found in (Sormani & Barnes 2019). Figure 3.8 shows the maximum emission of each pixel and gives a clear look at the distinctions between the brighter and dimmer regions of this gas cloud.

4.1.1 Velocity Discontinuity

A main point of interest that comes out of the moment maps is the velocity discontinuity found in Figure 3.4 within the NH_3 (3,3) map. This discontinuity was mentioned in Chapter 3 and is found in the separated region shown in red due to its high velocity. Within this smaller region, we see the velocity of the system go from ∼215$\mathrm{km\,s^{-1}}$ to ∼195$\mathrm{km\,s^{-1}}$ within the span of one pixel. When looking towards the center of the Milky Way, the closer you get to looking at the CMZ the more line-of-sight issues show up during data collection. This velocity discontinuity could therefore be a foreground gas cloud that is being picked up by the detectors. Besides foreground emission, the other reasons to observe velocity discontinuities come from the possibility of an inflow/outflow region. When observing jet inflows and outflows the velocities of the associated emission show up just as they have in Figure 3.4. However, this region does not show any signs of radio jets and this type of emission would show up in other maps. The most likely explanation for this velocity discontinuity is therefore two interacting gas clouds. Having two gas clouds that are actively colliding would produce velocity data that is being seen within this figure. When cross-referencing this idea with the moment 2 map (Figure 3.6) we see a more turbulent region of gas in essentially the same area for

the NH_3 (3,3) map. This turbulent region therefore also points to the possibility of this region being a region where multiple velocity components are colliding.

4.1.2 Rotation

Within Figure 3.4 we can see an extension of the main body of the cloud towards lower galactic latitudes. This extension is only highlighted in the NH_3 (1,1), (2,2), and (3,3) lines. Moving radially at $\sim 230\ \mathrm{km\,s^{-1}}$ this extension is moving around $30\ \mathrm{km\,s^{-1}}$ faster than the main body of the cloud.

Opposite rotation is also occurring within the main body of the pilot region gas cloud. Opposite rotation occurs due to the portion of the gas cloud at lower galactic longitudes having a lower velocity on average when compared to the rest of the cloud. This is the opposite to what I would expect due to the location of this gas cloud within the galaxy. Looking at Figure 1.2 we see that both the edge region and the pilot region are accreting into the center of the galaxy from the left to the right. So due to the direction of accretion and the size of the gas cloud, we would expect the right side of this cloud to have higher velocity structures when compared to the left. The fact that we do not observe this points to the possibility of there being an internal stretching going on within the cloud. There could have also been an initial torque applied to this system causing it to be observed in this unbalanced state. This counter-rotation is therefore a sign of turbulent gas. The turbulence could be a sign of currently ongoing or future star formation. I can discuss this possibility further when looking at how the temperature of the gas is organized.

4.1.3 Comparison with Infrared Herschel Data

The Herschel maps are shown in Figure 4.1 for the pilot region and in Figure 4.3 for the edge region. These two maps are contoured with the moment 8 map for each region showing off where emission from both the pilot region and the edge region show up in the Herschel infrared map. The wavelengths used by the Herschel space telescope map dust across a number of wavelength bands. Studying how this dust

is emitted in infrared wavelengths is important for the study of the early stages of star formation. As more energetic cores of molecular clouds emit photons, these energetic photons are absorbed by the surrounding dust and remitted at longer wavelengths. These longer wavelengths are often viewed in the infrared. Therefore seeing a strong correlation of structure with infrared maps yields information about the possibility of star formation. Within the pilot region specifically, we can see that there are multiple structures within this cloud that emit strongly within the 250 micron Herschel map and are also traced by the dense NH_3 gas as shown in the moment 0 maps (Figure 3.2). As you increase the map wavelength (shown at the top of each map) more emission penetrates through the interstellar gas that would otherwise block it. However, increasing your wavelength decreases your spatial resolution. So looking at the 350 micron map balances showing off emission that might not otherwise escape at shorter wavelengths, without becoming too washed out of detail like the 500 micron map. Within Figure 4.1 there is a clear correlation of the densest regions of the NH_3 map (labeled by the yellow contours) with the brightest infrared emission. There is also CO data of the pilot region. Figure 4.2 zooms out so we can see the more extended CO emission labeled by the green contours. Once again there is a strict spatial coherency with the denser NH_3 gas with the CO data. Something that is particularly interesting is the fact that at some of the brightest areas within the infrared maps, there are no CO emission pockets labeled by the contours. For example within Figure 4.2 in the 350 micron map there is a particularly bright infrared region at around 17h 56m of right ascension. In this bright infrared region, there is no concentration of CO. The denser NH_3 gas is the only area within these maps that shares strong spatial coherence with both the CO and infrared emission.

4.1.4 Pilot Region Column Densities and Temperature

From Figure 3.16 we can see a temperature of around $\sim$20K ($\pm$6.6K) for our "cold" temperature map which uses our NH_3 (1,1) and (2,2) transitions. We also see a temperature of $\sim$65K ($\pm$3.15K) for our "warm" temperature map which uses our NH_3 (2,2) and (4,4) transitions (Figure 3.17). These values are within the expected ranges for this region of the dust lanes because the gas is found to be around 5

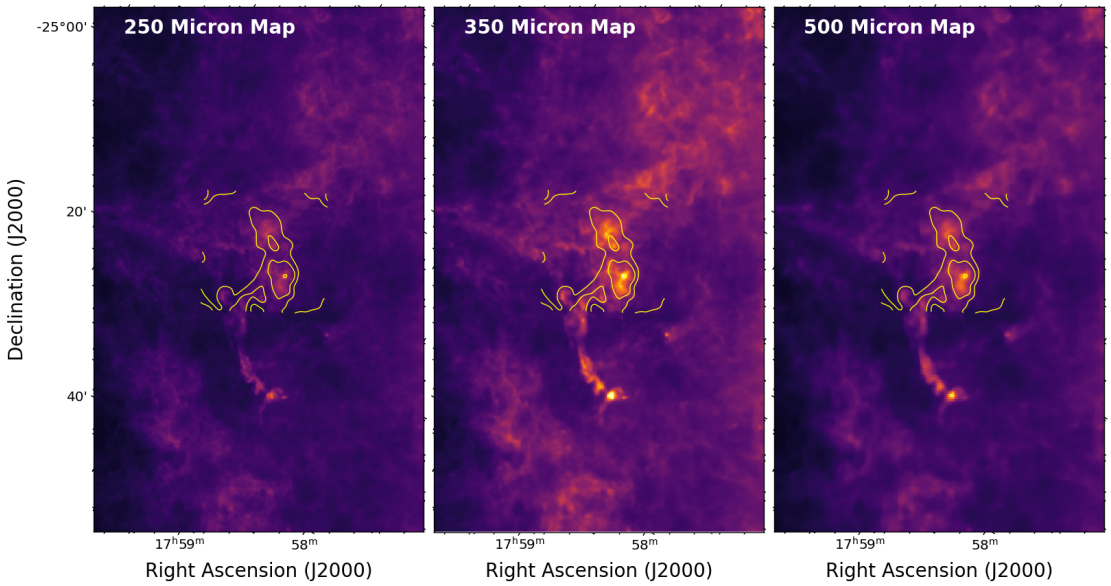

FIGURE 4.1: Pilot region shown in three different Herschel far infrared wavelengths labeled in the top left of each plot. The 250 micron map is shown from 152.97 to 3954.2 MJy/sr, the 350 micron map is shown from 69 to 1260 MJy/sr, and the 500 micron map is shown from 26 to 572 MJy/sr. The yellow contours are created from the NH_3 (1,1) pilot region moment 8 map.

K hotter than gas studied further out from the CMZ. This fact is shown when comparing the cold temperature map of the pilot region in Figure 3.16 and the cold temperature map of the edge region shown in Figure 3.18. As this gas accretes into the CMZ of the galaxy I expect its' temperature to increase (Ginsburg et al. 2016) which confirms the range for our findings. The topology of the pilot temperature maps is particularly interesting due to the apparent internal heating. Figure 3.16 and Figure 3.17 in Section 3 show warmer temperatures towards their centers. This could point to this being a possible star-forming region. Dense molecular gas such as NH_3 already suggests the possibility of future gravitational collapse. Hotter cores (T $\sim$ 100-300 K) of molecular gas have been known to be star-forming regions for massive stars (Osorio et al. 1999). So seeing internally heated dense molecular cores such as the ones that we see here suggests the possibility of the early stages of star formation. This would be caused by protostars increasing the temperature of the surrounding area through a release of gravitational energy as infalling gas and dust accrete onto possible protostars. It is important to keep in mind that since this was an exploratory project, there were no calibrator sources taken during the observing runs for both the pilot and the edge regions. This means

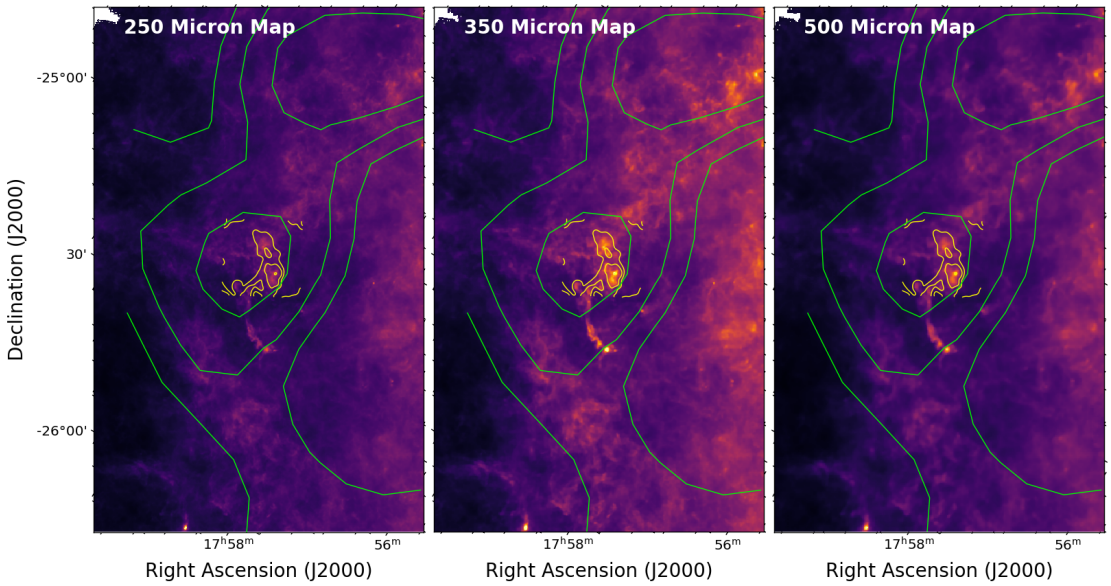

FIGURE 4.2: Pilot region shown in three different Herschel far infrared wavelengths labeled in the top left of each plot. The 250 micron map is shown from 152.97 to 3954.2 MJy/sr, the 350 micron map is shown from 69 to 1260 MJy/sr, and the 500 micron map is shown from 26 to 572 MJy/sr. The yellow contours are created from the NH_3 (1,1) pilot region moment 8 map. The green contours are created using the CO emission from Dame et al. (2001).

that the values of the temperatures are only important when being compared pixel to pixel.

4.2 Edge Region

To begin talking about the edge region it is good to first look at the moment 8 map displayed in Figure 3.9. Shown within the map is the maximum emission of each spectrum at each pixel. This shows where the gas is showing up brighter when compared with other parts of the same gas cloud. This gas cloud contains three brighter cores with streams of much fainter emission. These three brighter cores, along with the rest of the cloud show up in Figure 3.5 to have velocities of $\sim$130km s^{-1}. This can be directly compared with the CO emission found in Sormani & Barnes (2019) as denoted within the black box in Figure 1.2. The turbulence of the gas shows up in Figure 3.7 showing line widths between 0km s^{-1}

and $\sim$18km s^{-1}. This turbulence is on average larger than the turbulence associated with the pilot region. It seems that the edge region is much less complex and more isolated system than that of the pilot region.

4.2.1 Velocity Discontinuity

Just as in the pilot region, we see a velocity discontinuity within the edge region as shown in Figure 3.5. This region shows up in the NH_3 (1,1) emission map lower in galactic latitude than the rest of the cloud. This region stands out as having velocities of $\sim$115km s^{-1} when compared with the rest of the dim emission showing up as having velocities of $\sim$130km s^{-1}. Just as with the pilot region, the main conclusion of this discontinuity is the potential of there being multiple cloud components that are interacting and colliding creating a turbulent area of gas. There is also a possibility that this is not actually a physical source as we can compare the location of this discontinuity with the moment 8 map in Figure 3.9. The area this velocity discontinuity lies in is a low brightness region and so the emission is most likely washed out by noise.

4.2.2 Comparison with Infrared Herschel Data

Figure 4.3 shows the Herschel 250, 350, and 500 micron infrared maps contoured in cyan with the NH_3 (1,1) moment 8 map. Once again, just as with the pilot region, there is strong infrared emission coming from the region traced by the NH_3 contours. What is more interesting specifically with the edge region is that the infrared emission is stronger at the two points located at a right ascension of 18h 04m 50s and declination of -22°20'. These two emission hubs from the NH_3 data show up fainter than the main core located at a right ascension of 18h 04m 40s and declination of -22°17'. The distinct brightness of this region in comparison with the others is shown clearly in Figure 3.3. Zooming out we can better see the CO contours labeled in green within Figure 4.4. Once again there is a strong spatial coherence with the NH_3 gas and the CO gas, but not of the CO gas with the infrared. Particularly within the edge region maps, there is a region of infrared emission that is brighter than the area contoured by the NH_3 emission. This

brighter region of infrared is not contoured by the CO emission. The only location where the infrared emission is mapping to the CO emission is centered around the dense NH_3 gas of the edge region.

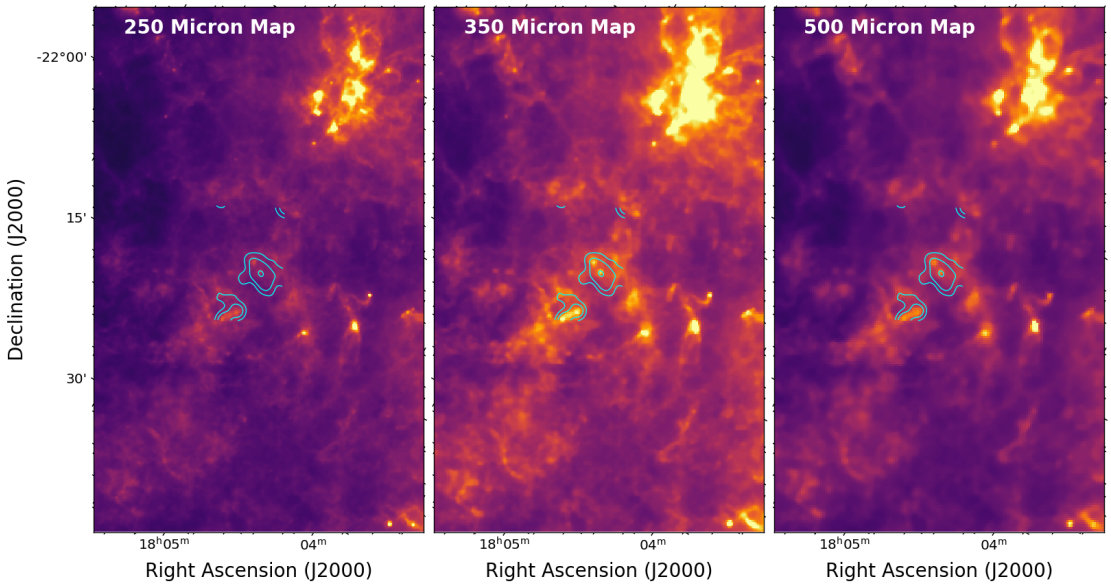

FIGURE 4.3: Edge region shown in three different Herschel far infrared wavelengths labeled in the top left of each plot. The 250 micron map is shown from 152.97 to 3954.2 MJy/sr, the 350 micron map is shown from 69 to 1260 MJy/sr, and the 500 micron map is shown from 26 to 572 MJy/sr. The cyan contours are created from the NH_3 (1,1) edge region moment 8 map.

4.2.3 Edge Region Column Densities and Temperature

The last interesting piece to look at with the edge region is the temperature map shown in Figure 3.18. We see here temperatures of about 18K in the hottest cores of the cloud. These temperatures are smaller than the temperatures found in the corresponding pilot region map shown in Figure 3.16. This figure shows the hottest cores with temperatures of around 23K. Given the contours on Figure 3.18 we do see a hotter core of the gas cloud, but it is not as much of a stark contrast with the edges of the cloud as it is within the pilot gas cloud. This suggests less efficient internal heating within the edge region as compared to the pilot region. The discussion of dendrograms will help better parse the possibility of a star forming region within the edge region gas cloud. As mentioned the Herschel data for the edge region was too dim to be able to make any physical

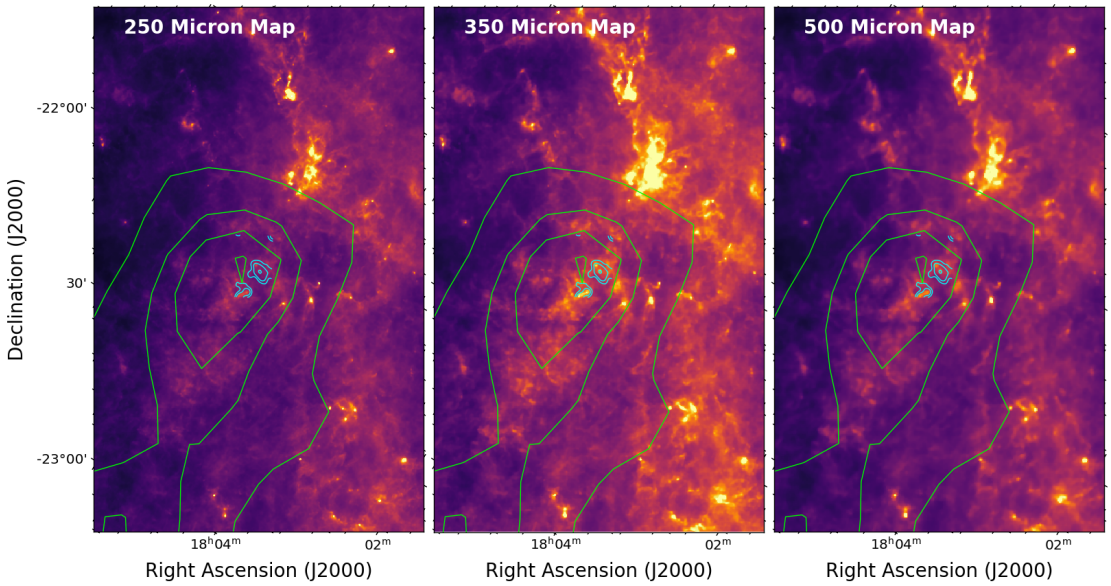

FIGURE 4.4: Edge region shown in three different Herschel far infrared wavelengths labeled in the top left of each plot. The 250 micron map is shown from 152.97 to 3954.2 MJy/sr, the 350 micron map is shown from 69 to 1260 MJy/sr, and the 500 micron map is shown from 26 to 572 MJy/sr. The cyan contours are created from the NH_3 (1,1) pilot region moment 8 map. The green contours are created using the CO emission from Dame et al. (2001).

conclusions and connections. Considering this along with how our moment maps for the edge region came out, it is good to assume that this region is much less complex structurally than the pilot region. The edge region is most likely a small dense clump of gas and dust that is just beginning its journey into the harsh and turbulent environment of the galactic center.

4.3 Dendrogram Analysis

It is very interesting to also compare the types of structures we see both within Figure 3.21 and Figure 3.23. The latter represents the edge region and there is much less complex structure when compared with the pilot region. For the edge region there seem to be three distinct cores shown within Figure 3.22 labeled in red, green, and yellow. However, when looking at Figure 3.23 it is shown that the green and yellow regions are a part of the same structure, and due to the way that the dendrograms are calculated, they are part of a self-contained velocity

grouping. When looking at Figure 4.3 we see these green and yellow structures showing up with essentially the same infrared brightness. From the dendrogram analysis and the comparison with the infrared map, these two spatially distinct cores are most likely interconnected. However, this seems to be the only grouping that has multiple structures connected to it within the edge region. The rest of the structures show up as their own leaves with no other associated structure. The orange structure is not physical and arises due to edge effects within the data cube. Therefore there is much less related structure within the edge region when compared with the pilot region. A conclusion of this comparison is the fact that the edge region shows up as a more isolated region than that of the pilot region within the NH_3 maps. However, we see similar concentrations of CO gas in Figure 4.4 as with the pilot region. Through these cross-references, I believe that the less structure within the edge region dendrograms arises from the smaller amount of data collected on the edge region.

The pilot region has many related structures when looking at Figure 3.21. This related structure leads to the conclusion that the pilot region is very interconnected within position-position-velocity space. The multiple connected structures of the dendrogram in Figure 3.21 that show up in Figure 3.20 as separate structures point to the idea of this system being interconnected. There is also an interesting comparison to be made with the moment 2 maps and the dendrogram structure. The line widths for the edge region are larger than those of the pilot region. This points to more turbulent gas within the edge region. This conclusion agrees with the edge dendrogram structures as shown in Figure 3.23. The lack of interconnected structure within this structure map means more turbulent and less interconnected gas within velocity space.

Another point of interest is comparing the maps of the dendrogram regions with their corresponding tables that give the v_{cen} of each region. As mentioned in Chapter 3 there are multiple components of each region that have the same location on the sky but have sometimes wildly varying v_{cen} values. When discussing the potential cause of this we must look back to the spectra as shown in Figure 3.1. This spectrum shows off the hyperfine structure as described in more detail in Chapter 1. As we iterate through each scan we look at the sky at a different frequency of light. Due to the hyperfine structure of NH_3 emission there are

multiple peaks rather than a normal Gaussian peak that would be seen in a CO data cube. Therefore it becomes increasingly difficult to compare and contrast these regions due to the fact that a peak at $100\mathrm{km\,s^{-1}}$ and a peak at $70\mathrm{km\,s^{-1}}$ will show up as two different regions within the dendrogram system.

CHAPTER 5: Conclusion

Galactic bar dust lanes act as galactic conveyor belts transporting gas and dust into the CMZ of their host galaxies. I study the midpoint and edge of the near-side dust lane of our own Milky Way bar. I find that the velocity of the midpoint gas cloud is around 205 $\mathrm{km\,s^{-1}}$ as it accretes into the center of the galaxy and the velocity of the edge region gas cloud is around 130 $\mathrm{km\,s^{-1}}$, which agrees with the expected values from Sormani & Barnes (2019). From equations found in Mauersberger et al. (2003) I am able to use two transitions of NH_3 to solve for the temperature of each of the systems. The temperature values found are shown in Figures 3.16, 3.17, and 3.18. These values agree with what I expect as there are relatively higher values in the midpoint region as compared to the edge region when using the same NH_3 transitions to create each map. The locations of hot cores within the pilot region suggest internal heating and the possibility of embedded star formation. This idea of embedded star formation agrees with the Herschel infrared data of the same region. There is a high spatial agreement between the NH_3, infrared, and CO emission for both the pilot and edge regions. Constructing a dendrogram analysis of the pilot region also shows that the gas cloud is made up of interconnected velocity components with denser cores of turbulent gas. The edge region is much more isolated compared to the pilot region and this means that it could be more likely to undergo gravitational collapse in the future. However, the infrared emission does not agree as much with the edge region as it does with the pilot region. In terms of dendrograms, the edge region is much simpler in structure when compared to the pilot region. Within the pilot region, we see many velocity components that can be structurally correlated even though they are separated in physical space. With the edge region, there seem to be essentially three more dense brighter cores and no other apparent interconnected structure.

For the future of this work, I will be looking back at the pilot region with the GBT during the 24A observing cycle with observer code GBT24A-329. This project proposal has been accepted and will be collecting data very soon. This future project will study the pilot region in many other molecular lines as well as radio recombination lines. The findings associated with the radio recombination lines

will help to confirm or refute the possibility of embedded star formation within the hot cores of gas within this region. This project I have undertaken is also just one step of a future project titled 'Bar Ammonia Radiation in Filaments, Lanes and YSOs Survey' (BARFLYS) which is being studied by Natalie Butterfield of the National Radio Astronomy Observatory. This overarching project will study and map the dust lanes from the disk of the galaxy to the CMZ in multiple NH_3 transitions. This will give observational data to describe the kinematics and temperature of the gas as it undergoes accretion.

APPENDIX A: Observation List

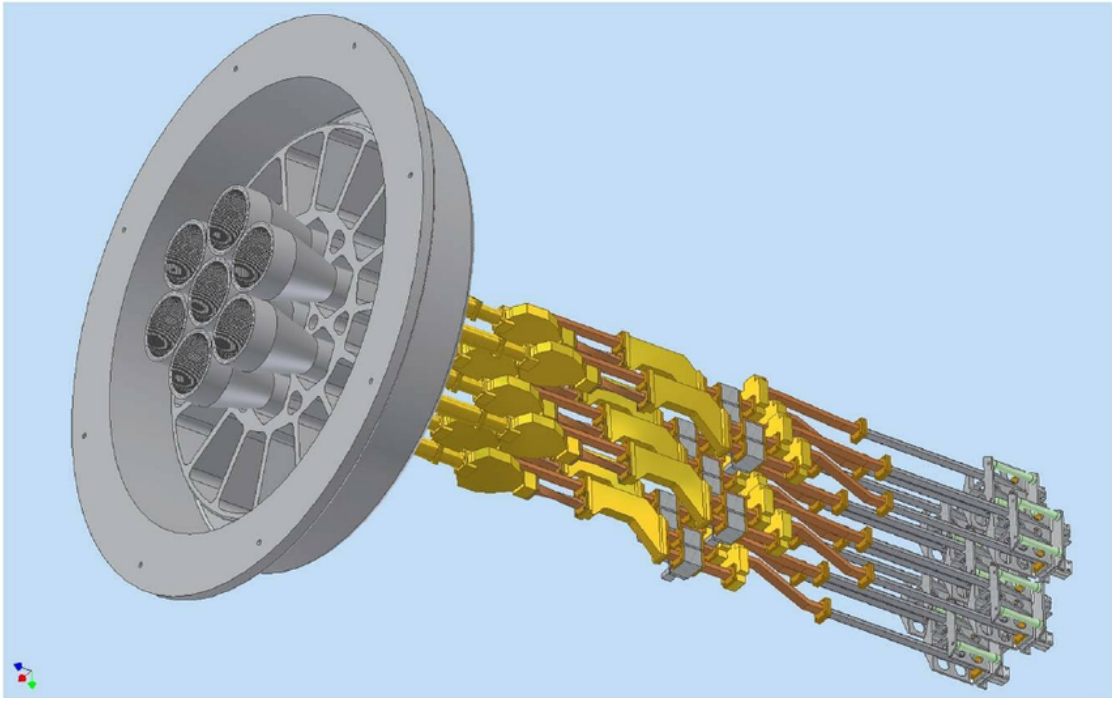

FIGURE A.1: Image showing the layout of the K-band Focal Plane Array containing the 7 constituent beams.

APPENDIX A: Bibliography

Athanassoula, E. 1992, MNRAS, 259, 345, doi: 10.1093/mnras/259.2.345

Bovy, J., Leung, H. W., Hunt, J. A. S., et al. 2019, MNRAS, 490, 4740, doi: 10.1093/mnras/stz2891

Cheung, A. C., Rank, D. M., Townes, C. H., Thornton, D. D., & Welch, W. J. 1968, Phys. Rev. Lett., 21, 1701, doi: 10.1103/PhysRevLett.21.1701

Dame, T. M., Hartmann, D., & Thaddeus, P. 2001, The Astrophysical Journal, 547, 792, doi: 10.1086/318388

de Vaucouleurs, G. 1964, in The Galaxy and the Magellanic Clouds, ed. F. J. Kerr, Vol. 20, 195

Debattista, V. P., Ness, M., Gonzalez, O. A., et al. 2017, MNRAS, 469, 1587, doi: 10.1093/mnras/stx947

Eskridge, P. B., Frogel, J. A., Pogge, R. W., et al. 2000, AJ, 119, 536, doi: 10.1086/301203

Fisher, D. B., & Drory, N. 2008, AJ, 136, 773, doi: 10.1088/0004-6256/136/2/773

Ginsburg, A., Henkel, C., Ao, Y., et al. 2016, A&A, 586, A50, doi: 10.1051/0004-6361/201526100

Ho, P. T. P., & Townes, C. H. 1983, ARA&A, 21, 239, doi: 10.1146/annurev.aa.21.090183.001323

Houlahan, P., & Scalo, J. 1992, ApJ, 393, 172, doi: 10.1086/171495

Kruijssen, J. M. D., Longmore, S. N., Elmegreen, B. G., et al. 2014, MNRAS, 440, 3370, doi: 10.1093/mnras/stu494

Mauersberger, R., Henkel, C., Weiß, A., Peck, A. B., & Hagiwara, Y. 2003, A&A, 403, 561, doi: 10.1051/0004-6361:20030386

Mills, E. A. C., & Morris, M. R. 2013, ApJ, 772, 105, doi: 10.1088/0004-637X/772/2/105

Miwa, T., & Noguchi, M. 1998, ApJ, 499, 149, doi: 10.1086/305611

Morgan, L. K., Figura, C. C., Urquhart, J. S., & Thompson, M. A. 2010, MNRAS, 408, 157, doi: 10.1111/j.1365-2966.2010.17134.x

Myers, P. C., & Benson, P. J. 1983, ApJ, 266, 309, doi: 10.1086/160780

Osorio, M., Lizano, S., & D'Alessio, P. 1999, ApJ, 525, 808, doi: 10.1086/307929

Ostriker, J. P., & Peebles, P. J. E. 1973, ApJ, 186, 467, doi: 10.1086/152513

Peschken, N., & Łokas, E. L. 2019, MNRAS, 483, 2721, doi: 10.1093/mnras/sty3277

Randers, G. 1942, ApJ, 95, 88, doi: 10.1086/144378

Rosolowsky, E. W., Pineda, J. E., Kauffmann, J., & Goodman, A. A. 2008, ApJ, 679, 1338, doi: 10.1086/587685

Sheth, K., Elmegreen, D. M., Elmegreen, B. G., et al. 2008, ApJ, 675, 1141, doi: 10.1086/524980

Sormani, M. C., & Barnes, A. T. 2019, MNRAS, 484, 1213, doi: 10.1093/mnras/stz046

Swade, D. A. 1989, ApJ, 345, 828, doi: 10.1086/167954

Toomre, A. 1964, ApJ, 139, 1217, doi: 10.1086/147861